UNIVERSITY OF CALIFORNIA, SAN DIEGO

Clinically-Guided Engineering for Scaling Wearable Health Monitoring: Stretchable Adhesive Sensors and Dynamic Statistical Analyses in Sleep Medicine

A dissertation submitted in partial satisfaction of the
requirements for the degree
Doctor of Philosophy

in

Bioengineering

by

Dae Y. Kang

Committee in charge:

Professor Todd P. Coleman, Chair
Professor Pedro J. Cabrales Arevalo
Professor James R. Friend
Professor David A. Gough
Professor Atul Malhotra
Professor Robert L. Owens

2017

The dissertation of Dae Y. Kang is approved, and it is acceptable in quality and form for publication on microfilm and electronically:

_____

_____

_____

_____

_____

_____

Chair

University of California, San Diego

2017

EPIGRAPH

To Mom,
For raising me with love.

To the Fam,
For keeping me grounded and true.

To Zarina,
For inspiring and loving me.

EPIGRAPH

I love sleep.
My life has a tendency to to fall apart when I'm awake,
you know?
—Ernest Hemingway

TABLE OF CONTENTS

LIST OF FIGURES

LIST OF TABLES

Very Special Thanks To...

Zarina: For being my champion. These last few years have been a roller coaster of emotions, life decisions, and growth. We have evolved as individuals and as a couple, and I can't articulate how incredibly vital you have been to all I've accomplished. If I was down on my research, you rallied me up. If I was up on a small win, you would celebrate with me. You know me and my endeavors uniquely, and I am grateful for your steadfast love, support, and compassion. You should receive a Ph.D. in The Dynamic Analysis of A Ph.D. Student. Thank you for seeing my potential as a (then) kid from the hood, for standing by my side, for making sure I keep sight of the important things in life, and for forming me into an intuition-inclined engineer. My accomplishments are your accomplishments.

Mom: For being an unwavering source of inspiration, for being both Mom and Dad. For as long as I can remember, you have demonstrated a work ethic and genuine curiosity that I admire so greatly. Even after you got sick, you somehow bounced back and continued school, continued pursuing what you love to do. If I could have half as much grit and perseverance as you, I might win a Nobel Prize one day. You always told me, "Querer es poder." Those words always ring with me through good and bad times. Thank you for never giving up, and for being a primary source of inspiration in my pursuit of knowledge.

My Familia: For being the constant, solid foundation in my life. Every one of you reminds me of my roots, my motivations to be a good person and a good mentor to the young ones and others from different walks of life. Thank you for always being there, even though I've decided to go on this crazy adventure in education and research. My hope has always been to serve as an example of what we are all capable of — that a bit of work and luck allows us to accomplish whatever makes us tick in life.

Tubby (Pig h.D) & Trey (Bagel): For listening to my thoughts and rants, without judgment. Only ever responding with licks, requests for scratches, and wagging tails.

Todd: For all the invaluable mentorship and unrestricted motivation to pursue what I found interesting. You made the pursuit of a doctorate, I feel, a very unique experience, for which I am profoundly grateful.

Diego, Armen, and Yun Soung (aka Team Coleman): For all the bike rides, procrastination, motivation, and inspiration. I couldn't have hand-picked a better group of fellas to earn a Ph.D. with.

The Neural Interaction Laboratory: For being an amalgam of humor, intellect, and compassion. So many interesting, compelling people go through this lab — I will miss the procrastinating through insightful discussions around the water cooler.

The National Science Foundation and the National Institutes of Health: For providing research funding and support throughout my graduate career, through the NSF GRFP, NIGMS R25, and the NHLBI R01 Diversity Supplement mechanisms.

Co-Authors and Publishers

Chapter 2, in full, is a reprint of the material as it appears in *Sensors* 2015. Kang, Dae Y.; Kim, Yun Soung; Ornelas, Gladys; Sinha, Mridu; Naidu, Keerthiga; Coleman, Todd P., MDPI AG, 2015. The dissertation author was the primary investigator and author of this paper.

Chapter 3, in full, is a reprint of the material as it appears in *IEEE Transactions on Biomedical Engineering* 2017. Kang, Dae Y.; DeYoung, Pamela N.; Malhotra, Atul; Owens, Robert L.; Coleman, Todd P., IEEE, 2017. The dissertation author was the primary investigator and author of this paper.

Chapter 4, in part is currently being prepared for submission for publication of the material. Kang, Dae Y.; Malhotra, Atul; Owens, Robert L.; Coleman, Todd

P. The dissertation author was the primary investigator and author of this material.

VITA

2012	B. S. in Bioengineering, University of California, San Diego
2012-2017	Mentor and Education Facilitator, IDEA Engineering Student Center, University of California, San Diego
2017	Ph. D. in Bioengineering, University of California, San Diego

PUBLICATIONS

Kang, D.Y., DeYoung, P.N., Malhotra, A., Owens, R.L., Coleman, T.P. (2017). "A State Space and Density Estimation Framework for Sleep Staging in Obstructive Sleep Apnea," *In Press, IEEE Trans. Biomed. Eng.*, 2017.

Coleman, T.P., Tantiongloc, J., Alegra, A., Mesa, D., **Kang, D.Y.**, Mendoza, M. (2016). "Diffeomorphism Learning via Relative Entropy Constrained Optimal Transport," *2016 IEEE Global Conference on Signal and Information Processing.*

Onton, J., **Kang, D.Y.**, Coleman, T.P. (2016). "Visualization of whole-night sleep EEG from 2-channel mobile recording device reveals distinct deep sleep stages with differential electrodermal activity," *Front. Hum. Neurosci.*, 10(605), doi: 10.3389/fnhum.2016.00605.

Kang, D.Y., Kim, Y.-S., Ornelas, G., Sinha, M., Naidu, K. Coleman, T.P. (2015). "Scalable Microfabrication Procedures for Adhesive-Integrated Flexible and Stretchable Electronic Sensors," *Sensors*, 15(9), 23459-23476.

Kagan, D., Balasubramanian, S. Hu, C., Campuzano, S., Lobo-Castaon, M., Lim, L., **Kang, D.Y.**, Zimmerman, M., Zhang, L. Wang, J. (2011). "Micromachine-Enabled Capture and Isolation of Cancer Cells in Complex Media," *Angew. Chem. Int. Ed.*, 50(18), 4161-4164.

Kagan, D., Laocharoensuk, R., Zimmerman, M., Clauson, C., Balasubramanian, S., **Kang, D.Y.**, Bishop, D., Sattayasamitsathit, S., Zhang, L., Wang, J. (2010). "Rapid Delivery of Drug Carriers Propelled and Navigated by Catalytic Nanoshuttles," *Small*, 6(23), 2741-2747.

ABSTRACT OF THE DISSERTATION

Clinically-Guided Engineering for Scaling Wearable Health Monitoring: Stretchable Adhesive Sensors and Dynamic Statistical Analyses in Sleep Medicine

by

Dae Y. Kang

Doctor of Philosophy in Bioengineering

University of California, San Diego, 2017

Professor Todd P. Coleman, Chair

Background & Objective: Although the reasons behind the biological necessity of sleep remain to be fully discovered, emerging data show that sleep is crucial for maintaining physical health and mental well-being. Despite its great importance, nearly 40% of US adults experience problems with sleep, ranging from sleep deprivation (decreased total sleep time) to sleep disorders (e.g. obstructive sleep apnea, OSA). Furthermore, many millions of these individuals with sleep disorders are severely underdiagnosed. The major limitation to improved understanding of sleep in health, and streamlined identification of at-risk individuals, is the inability to objectively measure sleep at scale. Gold standard sleep mea-

surement by polysomnography (PSG) requires bulky, obtrusive measurements of multiple biological signals that interfere with sleep. Analysis of sleep measurements undergo a manual/visual process that is lengthy, expensive, and subjective. These impediments to sleep make testing beyond a single night in selected patients impractical, and make addressing growing public health issues in sleep seemingly impossible. **Methods & Results:** To address these shortcomings in the current sleep medicine paradigm, a systems approach to clinically-guided engineering spanning sensing and analytical aspects of sleep monitoring is described herein. Adhesive-integrated stretchable sensors were engineered to achieve scalable, peel-and-stick sensing on ubiquitously used clinical adhesives, resulting in a cost-effective, facile, and familiar means for clinical implementation of unobtrusive electrophysiological sensors. Simultaneously and in collaboration with sleep medicine clinicians, small-data statistical analytics were engineered to dynamically assess clinical-grade sleep architecture from single-channel electrophysiology, the results of which are on par with in-lab PSG for both healthy/normal individuals and patients with OSA. **Conclusion & Significance:** The result of this applied clinical engineering research is a suite of tools that emphasizes miniaturization of sleep sensing methods, complemented by analytical endeavors to generate clinical-grade sleep measures from consequential small-data platforms. The gestalt is not only envisioned for objective assessment of sleep-based clinical outcomes, but to also stimulate basic science investigation of sleep dynamics and their context in other comorbidities. By performing engineering in medicine in a systemic manner, the principles of this work show potential for extrapolation to advance general wearable health monitoring practice.

Chapter 1

Introduction

1.1 Sleep and its Growing Role in Healthcare

Healthcare has increasingly become the new frontier, with many advances in this space spurred by endeavors in mobile health technologies, materials science/engineering, and an improved understanding of how these systems can interface with the human body. Combined with the notion that more and more individuals are seen as "unhealthy" or "at-risk" of certain ailments, the state of healthcare is experiencing a shift to value-based care and a promise of enabling personalized medicine to address an increasingly diseased population. For example, the World Health Organization estimates that the incidence of cancer will increase from 14 million patients in 2012 to 22 million in 2032 [1]. Incidence of diabetes, another increasing and seemingly common disease, is expected to jump from 382 million patients to 592 million within a similar time span [1].

With these public health issues at bay, and many more to be brought to light and/or discovered, many now look to invest in and adopt high-tech medical technologies and data-driven medicine, as a means for improving and advancing the methods by which medicine is performed. An example of this is the establishment of the Precision Medicine Initiative/All of Us Research Program [2], one of the many initiatives that seeks to maximize the effectiveness of medicine through increased understanding of genes, environmental factors, and characteristics of daily lifestyle. Interestingly, such endeavors seek to consult physiologic phenomena typ-

ically reticent in medicine, but increasingly discussed in a health context, such as the process of sleep [2].

Sleep and sleep quality data, among other dynamic physiological data, are now being considered as instrumental in assessing arbitrary disease risk and severity [2]. Continuous monitoring of sleep data has become somewhat commoditized through the expansion of the wearable device market and adoption of mobile health technologies. This comes with good reason, for as many as 50-70 million U.S. adults suffer from chronic lack of sleep and/or sleep disorders [3]. A recent study performed by the Centers for Disease Control found that an average of 36.5% of currently employed adults report short sleep duration, or persistent sleep deprivation. Of the many major occupations sampled, those with the highest prevalence of short sleep duration were production workers, food service workers, and — ironically enough — healthcare supporters and practitioners [4]. To focus on a pending public health issue, approximately 20% of U.S. adults are suspected of suffering from obstructive sleep apnea (OSA), a sleep breathing disorder characterized by a chronic partial or complete cessation of breathing during sleep [5]. Left untreated, OSA can lead to increased risk of hypertension, stroke, diabetes, and work-related accidents (Figure. 1.1) [5, 6]. The intermittent state of hypoxia induced by OSA and other sleep breathing disorders has been found to be strongly associated with cancer mortality, even after accounting for possible confounding variables such as age, body-mass index, and diabetes [7]. Suffice it to say, the pervasiveness of OSA, its correlation with some of society's most pressing health issues, and a general trend toward societal sleep deprivation, suggests that sleep plays a vital role in maintaining good physical and mental health.

Sleep, though its specific mechanisms are still relatively unknown, can generally be described as a human state during which one observes a quiescence of normal "wakeful" behavior. Physiologically, the human brain undergoes a series of cyclical transitions between synchonrous and asynchronous electrical activity, associated with changes in cardio-respiratory dynamics and skeletal muscle tonicity, among other things. These cycles of physiologic change occur on the order of every 90-110 minutes, at least in healthy adult individuals [8]. Standard measures of

these physiological signals are performed through the use of engineered biomedical tools/methods, such as electroencephalography (EEG), electromyography (EMG), pulse oximetry, and thermistor-based temperature and respiratory flow measures, to name a few. Each signal provides insight into certain physiologic processes (e.g. brain oscillations, muscle activation, blood flow), which are then used to abstract certain qualities and characteristics of the sleep process [8].

Figure 1.1: Chronic sleep deprivation and sleep fragmentation can cause (and be caused by) a number of pathologies, increasing risk of chronic comorbidities and overall decrease in quality of life.

1.2 The Current Sleep Medicine Paradigm: Room for Improvement

Taken together, the gold standard method by which clinicians assess sleep is through the in-lab polysomnogram (PSG), which incorporates the above mentioned signals (alongside others) to estimate and categorize different sleep states, so termed the stages of sleep (Figure 1.2) [8]. A variety of sensors are positioned from head-to-toe on the body to record relevant sleep physiology throughout the

course of the night. These many data streams are then interpreted by a skilled technician and/or clinician to "score" and condense every 30 second window of sleep biosignals into a single designation related to predefined sleep states, the so called stages of sleep. In 1968, Rechtschaffen and Kales published the first designations for categorizing these seemingly discrete sleep states [9]. Since then, the interpretation and classification of sleep biosignals into such stages has been revised and discussed many times over, ultimately leading to our modern day 5-stage sleep paradigm – stages Wake, Rapid Eye Movement (REM) sleep, N1 (light/drowsy) sleep, N2 sleep, and N3 (deep) sleep [10].

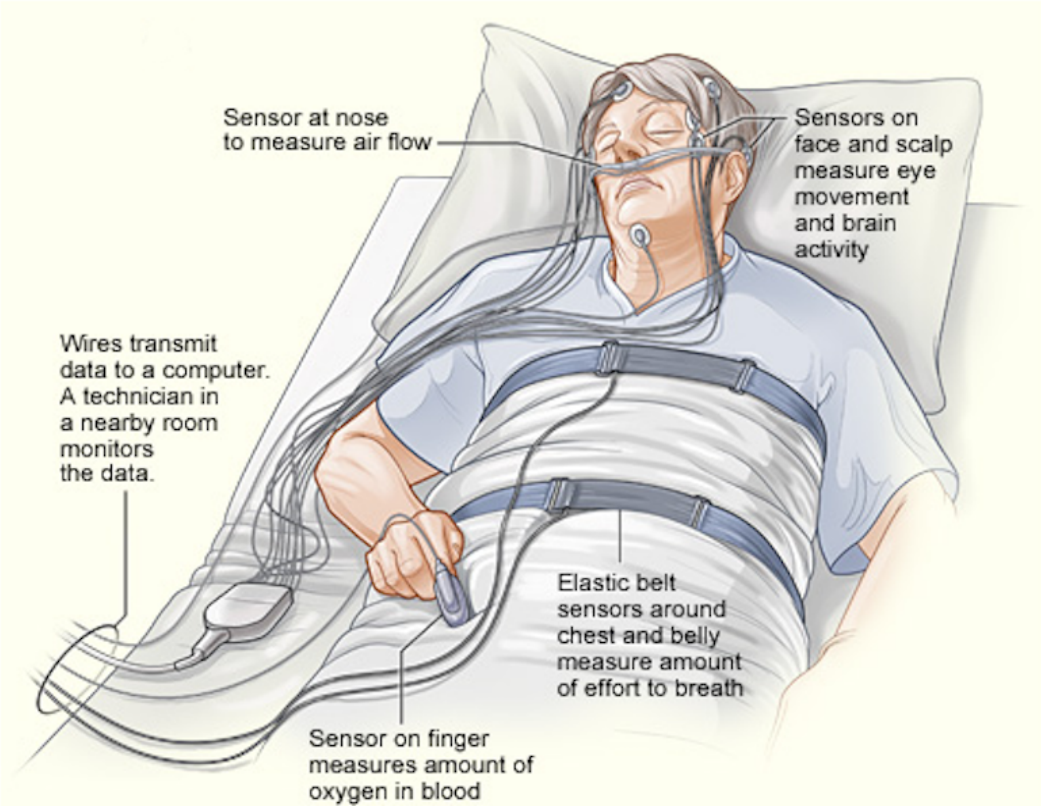

Figure 1.2: The conventional in-lab polysomnogram (PSG) sleep monitoring paradigm. The PSG typically consists of multiple physiological measures including brain, heart, and muscle electrophysiology, measures of respiration and air flow, and measures of blood circulation/oxygenation. All signals are recorded continuously through the course of the night, for at least one overnight, in-lab sleep study.

With these 5 designations of sleep, a trained clinician and/or technician is

able to visually/manually classify the many windows of data acquired throughout the night to generate a hypnogram – a plot of sleep trajectory through the five sleep stages, as a function of time (Figure 1.3). At each sleep window, a sleep patient is to occupy a single arbitrary stage of sleep, and more or less transitions between these sleep stages throughout the course of the night. The macrostructure of this whole-night sleep architecture gives the clinician an indication of sleep quality, through certain metrics extracted directly from the hypnogram, such as total sleep time, sleep efficiency, and sleep latency [11]. For example, values of total sleep time close to the total recording time might indicate a restful night of sleep. Conversely, decreased total sleep time could suggest that the patient exhibits sleep deprivation, perhaps due in part to a sleep disorder such as insomnia. A closer look at the hypnogram and its microstructure might reveal frequent arousals to wakefulness from sleep (i.e. sleep fragmentation), thus causing an inability to achieve N3 deep, restorative sleep, such as in OSA.

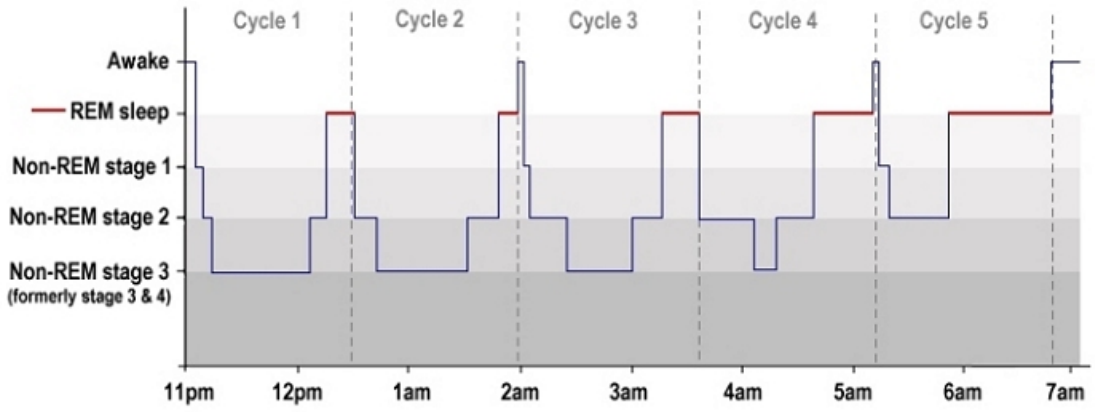

Figure 1.3: A typical sleep hypnogram of healthy sleep. Sleep begins in the awake state, and transitions through all five clinically-relevant stages throughout the night. A healthy individual experiences staircase-like sleep cycles of approximately 90-110 minutes, until awakening some 7-8 hours later.

Such insights can be gleaned from the sleep hypnogram, and therefore from the PSG-based sensing and analysis of relevant biosignals during sleep. While this method has proven immensely helpful in elucidating the mechanisms and significance of sleep , sleep medicine and research has come to require improved methods

for assessing sleep objectively and at scale. The PSG's many-sensors montage, in concert with the cumbersome and subjective visual interpretation of physiological signals, is not practical for addressing the growing interest and need in sleep monitoring and sleep disorder diagnostics (Figure 1.3). In the U.S. alone, over 1 million in-lab clinical PSGs are performed each year [12]. Still, approximately 80-90% of individuals suspected of having OSA (30-35 million individuals) are undiagnosed [13]. To make matters worse, sleep scoring agreement between experts is only about 80%, with declining agreement when scoring sleep in individuals with sleep disorders [14]. This inherent variability in scoring accuracy leads to re-testing and increased risk of false positives/negatives, further exacerbating the disparity of assessing sleep at scale. With associated comorbidities to OSA increasing — such as the rise in both adult and childhood obesity – one suspects that the standard in-lab scheme cannot keep pace with increasingly undiagnosed individuals. Furthermore, the lack of robust sleep measures stymies the research community and its ability to investigate the underpinnings — and therefore the mechanics and significance — of the sleep process. Some topics of interest here are the investigation of sleep phenotypes, sleep dynamics within and across sleep disorders, and the characteristics of sleep in other seemingly unrelated pathologies. The "not-yet-applied" research, in this regard, cannot be performed to inform new clinical understanding of sleep in the context of human health. In short, the "gold" standard PSG — from sensing of sleep signals to their analysis and interpretation — appears more as more of a "bronze" standard.

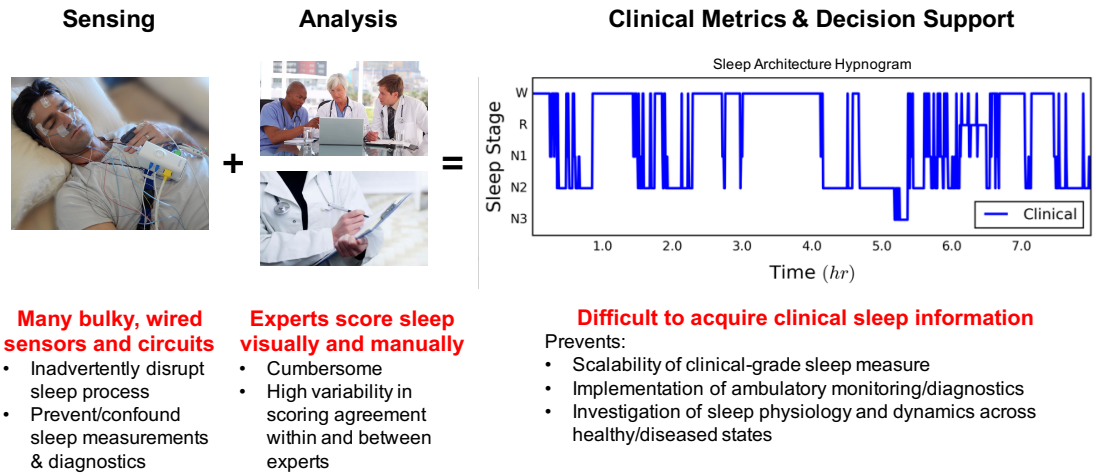

Figure 1.4: Shortcomings of conventional sleep monitoring and diagnostics.

1.3 Thesis: Engineering of Stretchable Sensing Technology and Low-Resource Analytics for Scalable Clinical Sleep Monitoring

As discussed, the major limitation to improved understanding of sleep in health, and streamlined identification of at-risk individuals, is the inability to objectively measure sleep at scale. The reasons for this are two-fold: 1) Gold standard sleep measurement by PSG requires bulky, obtrusive measurements of multiple physiological signals that interfere with sleep and 2) Analysis of subsequent sleep measurements undergo a labor intensive and subjective scoring process.

Herein I discuss a suite of research work that aims to develop both sensing and analytic tools for objective and scalable implementation in Sleep Medicine. Chapter 2 discusses the unconventional microfabrication and testing of stretchable sensors that are integrated into clinical adhesives, for simple, peel-and-stick acquisition of physiological data. Chapter 3 goes on to discuss the utility of state space modeling and statistical estimation for automated whole-night sleep staging from single channel electrophysiology. Chapter 4 presents current work improving upon the previous chapters and extrapolating the methods described to create

new sensors and analytics for specific sleep monitoring and diagnostic applications. Both sensors and analytics implemented in concert could potentially open new avenues for clinicians to engage patients in and beyond the hospital, investigate other poorly understood sleep-related pathologies, and update/develop operations and policy for improving clinical outcomes. The gestalt is engineering motivated by applied clinical research and collaboration, with the goal of exemplifying the significance of engineering in Sleep Medicine.

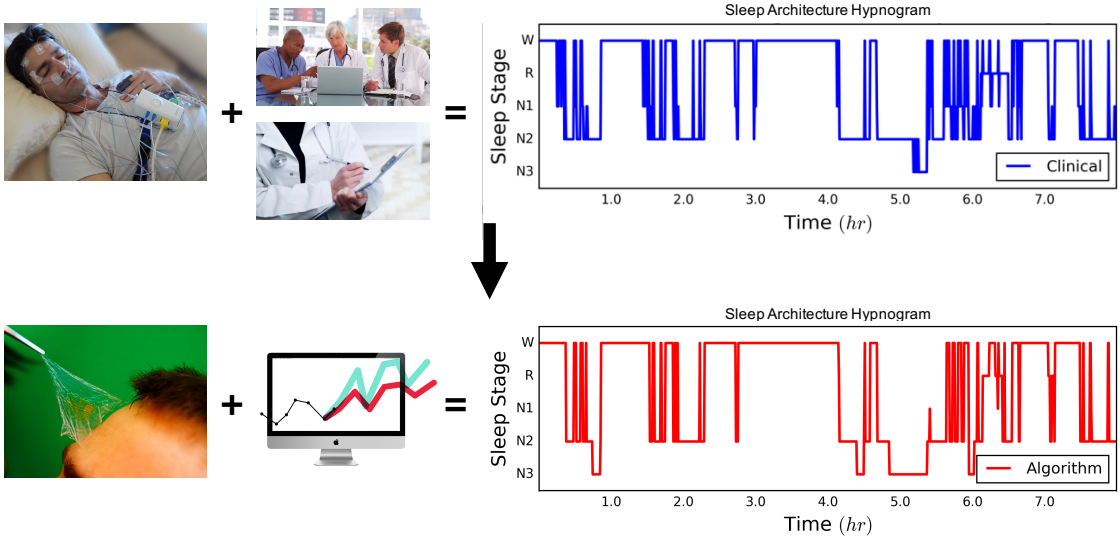

Figure 1.5: Co-development of stretchable sensors and sleep analytics for improving sleep monitoring.

1.4 Acknowledgements

Disclaimer: all figures in Chapter 1 consist of at least one image, which were found through Google image search of relevant term, and were modified slightly for the purposes of this dissertation. They are not property of the dissertation author or his co-authors.

Chapter 2

Scalable Microfabrication Procedures for Adhesive-Integrated Stretchable Electronic Sensors

Chapter 2 presents research findings previously published in Kang, D.Y. et al. 2015 [15]. Here, I delineate my work on stretchable sensors, microfabricated and designed to integrate into clinical adhesives. This piece represents a response to the first issue with current sleep monitoring practices, namely the inability to sense sleep biosignals in a scalable and minimally-irksome manner.

2.1 Abstract

New classes of ultrathin flexible and stretchable devices have changed the way modern electronics are designed to interact with their target systems. Though more and more novel technologies surface and steer the way we think about future electronics, there exists an unmet need in regards to optimizing the fabrication procedures for these devices so that large-scale industrial translation is realistic. This article presents an unconventional approach for facile microfabrication and

processing of adhesive-peeled (AP) flexible sensors. By assembling AP sensors on a weakly-adhering substrate in an inverted fashion, we demonstrate a procedure with 50% reduced end-to-end processing time that achieves greater levels of fabrication yield. The methodology is used to demonstrate the fabrication of electrical and mechanical flexible AP sensors that are peeled-off their carrier substrates by consumer adhesives. In using this approach, we outline the manner by which adhesion is maintained and buckling is reduced for gold film processing on polydimethylsiloxane substrates. In addition, we demonstrate the compatibility of our methodology with large-scale post-processing using a roll-to-roll approach.

2.2 Introduction

Flexible and stretchable electronics systems – comprised of sensors and circuitry – are increasingly deemed relevant to the future of industrial and consumer electronics devices. The evolution of bulky and rigid electronics into their thin and unobtrusive counterparts has required innovative techniques going beyond standard implementations of CMOS microfabrication. Of these, screen-printing techniques achieve low-cost and scalable processing of flexible sensors and systems [16–22], though some devices lack the potential for fully integrated electronics with ultra-thin profiles. Engineering of thin film nanocomposites is another example of this trend in miniaturizing our every-day electronic devices [23–42]. Within this class, electronics systems utilizing sacrificial layers (e.g. poly(acrylic acid) (PAA), poly(sodium 4-styrene sulfonate) (PSSNa), poly(n-vinylpyrrolidone) (PVP), poly(methyl methacrylate) (PMMA), water soluble tape, Silicon (Si), SiO2) [43–46] and intermediate substrates (e.g. polydimethylsiloxane (PDMS), water soluble tapes) for transfer printing have allowed for nanomembranes with mechanically-tuned properties [23–32, 47]. For example, epidermal electronics systems boast ultra-thin, high resolution, skin-like sensors and circuitry designed for conformal lamination onto the skin [23–27,29–31]. These systems excel in the area of intimate integration with contoured and elastic real estates, as compared to traditionally rigid or thin film sheet devices that are otherwise too inflexible and/or unstretch-

able. The result is robust skin-electrode contact yielding prolonged biosignal acquisition with reduced motion artifact [48]. Overall, these electronics present many significant advances for mobile technologies, but the manner in which they are fabricated requires intermediate materials, and precision involved in transfer printing in order to produce high yields.

A demand for tomorrows inconspicuous sensors is quickly rising, in particular due to the advent of wearable devices and the Internet of Things (IoT) – a paradigm emphasizing data interconnectedness through the omnipresence of networked sensors and systems. This is exemplified by the five-fold increase in sensors from 2012, resulting in 23.6 billion sensors in 2014 [49]. Unfortunately, these numbers are accompanied by the high cost and complexity of fabricating minimally obtrusive sensors, which proves to be a barrier for widespread adoption of IoT practices in spaces such as healthcare, home, and industrial use [49, 50].

Herein we describe an alternative microfabrication approach requiring approximately half the steps of previous approaches to build similar devices. This reduction in steps has multiple benefits, including higher yield, lower cost. Also, the elimination of crucial steps enables new opportunities for large-scale production. This new approach uses a weakly-adhering interface and inverted fabrication scheme, which obviate the need of a sacrificial layer or intermediate transfer printing, and allow for direct integration of the sensor from the donor substrate to target receiving adhesive. Direct integration without transfer printing is facilitated by a simple mechanical peel-off step – similar in nature to the methods used for exfoliation of graphene and other materials [51–54], except that a complete device is peeled and packaged without requiring further microfabrication steps. Resulting adhesive-peeled (AP) sensors are used to record electrophysiological signals and results compared to those of a transfer printing approach [23–28], demonstrating similar sensor fidelity while emphasizing a simple peel-off technique that has potential for industry-scale roll-to-roll post-processing.

2.3 Methodology

2.3.1 Process Description

Throughout this discussion, we consider approaches that result in a sensor of pre-specified geometry to be embedded within a given adhesive. The purpose of this work is to facilitate a process by which the same or similar sensor can be made more easily and with higher yield. We compare an approach that utilizes transfer printing (TP) of passive sensors to a new methodology presented herein. To differentiate the two, sensors produced by the TP approach are designated as TP sensors, while the presented approach yields AP sensors.

Figure 2.1 provides a conceptual description of the two approaches. The TP process (top) begins with a donor substrate and undergoes a string of standard cleanroom procedures, which includes depositing a sacrificial layer (e.g. PMMA). The donor substrate then is dipped in solvent (e.g. acetone) that dissolves the sacrificial layer and separates the carrier substrate from the other deposited materials. Subsequently, two transferring steps ensue through which the desired pattern is delivered to an intermediate transfer material (e.g. PDMS), and then upon pressure, finally onto a target receiving substrate. This process path culminates in an adhesive with a patterned metal-polymer stack ready for use. The AP process (bottom) obviates the need for depositing a sacrificial layer or intermediate transfer printing and allows for direct application of the adhesive onto the donor substrate to embed the pattern within the adhesive. The AP process accomplishes this reduction in steps and direct transfer to the adhesive through the use of: 1) a weakly-adhering donor substrate and 2) inverted production of the metal-polymer stacks comprising the sensors. The rationale for this approach will be elucidated in the Discussion section.

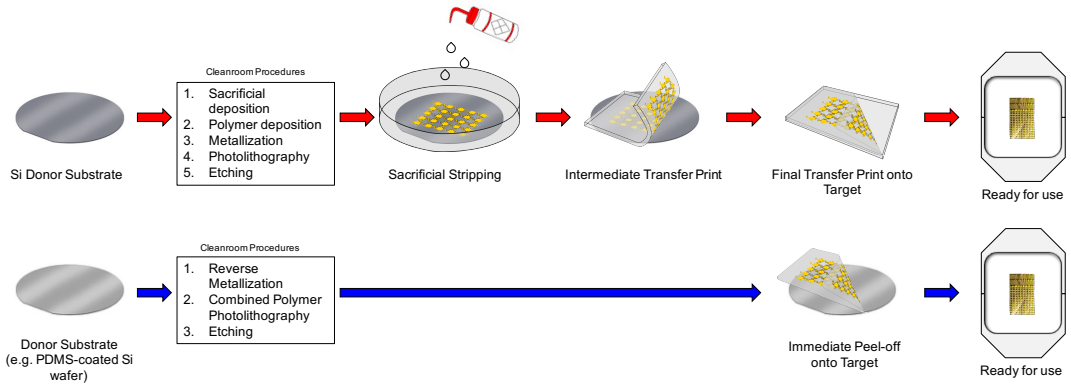

Figure 2.1: Example of TP vs. AP processes. **Top:** TP process steps, starting with Si donor substrate. Includes procedures such as depositing a sacrificial layer, using solvent for stripping sacrificial layer, and transfer printing by an intermediate elastomeric substrate; **Bottom:** AP process obviates the need for sacrificial layer, use of solvents, or use of an intermediate elastomer for transfer printing. Instead, a weakly-adhering donor is used, from which reversed metallization and a combined polymer deposition and photolithography step are implemented to create an inverted sensor. Because the sensor is inverted on a weakly-adhering surface, peel-off is performed directly by adhesive. Both processes result in the same sensor embedded within adhesive; the latter requires fewer steps and materials.

2.3.2 Fabrication of AP Sensors

The process for fabrication of AP sensors is illustrated in Figure 2.2. An example for results in this narrative is as follows. A standard Si wafer is coated with a thin silicone layer, creating a weakly-adhering interface, which comprises the donor substrate (Figure 2.2a). Standard cleanroom techniques are applied in a semi-reversed order for creating inverted flexible sensors on the donor substrate. Sequential metallization of gold (Au) and chromium (Cr) thin films onto PDMS form the conductive layer of these sensors (Figure 2.2b): the Au thin film interfaces with the weakly-adhering donor while Cr is exposed at the top. A photodefinable polyimide (PPI) is then used for simultaneous formation and patterning of the sensors polymer backing (Figure 2.2c). An etch-back of the exposed Cr-Au regions (Figure 2.2d) results in a donor substrate with AP sensors that can be directly peeled-off by the adhesive of choice (Figure 2.2e,f).

Specifically, formation of the weak-adhering donor substrate is prepared by

spin coating and curing a 50μm thick layer of poly(dimethylsiloxane) (PDMS; Sylgard 184, Dow Corning, Midland, MI, USA) onto a 4-inch silicon or glass wafer (University Wafer, USA). Thin metal films are deposited on top of the PDMS surface using either a sputter system (ATC Orion, AJA, USA) or electron beam (e-beam) evaporator (Temescal BJD 1800, Ferrotec, Santa Clara, CA, USA) to form Au and Cr metal layers (in this order) of 200nm and 5nm in the thicknesses, respectively. A negative-tone photodefinable polyimide (HD-4104, HD Microsystems (Dupont), Wilmington, DE, USA) is spin coated at 3,000 revolutions-per-min for 1 min, soft baked (150°C, 1 min), and UV-exposed (EVG620, EV Group, Sankt Florian am Inn, Austria). The polyimide layer is developed by using a modified puddle approach found in the literature [55]. The photodefined polyimide (resting on top of the wafer) is placed in a convection oven (Carbolite, Derbyshire, UK) at 250°C for 90 min to ensure full curing of the polyimide patterns and complete bonding to the interfacing Cr layer. The wafer is then dipped in Cr and Au etchants (Transene, Danvers, MA, USA) (in this order) to remove unnecessary metal surfaces, only leaving metal layers directly under the polyimide pattern intact. Completed devices are peeled onto the target receiving substrate, such as Tegaderm (3M, Saint Paul, MN, USA), by laminating the target adhesive film over the devices and delaminating once the device is adhered. Overall process time – starting with 3 pre-PDMS donor substrates and ending with completely peeled devices from 3 donors – is approximately 5 hours. Fabrication of AP sensors on flex substrate follows the same method, except that 25μm Kapton film (DuPont, Wilmington, DE, USA) is used as the donor substrate. For TP sensors, a streamlined version of the fabrication procedures outlined in [23] were used. Under the same experimental conditions and same number of sensors, the end-to-end TP process (from unmodified donor substrate to post-transfer printing) is approximately 10 hours long.

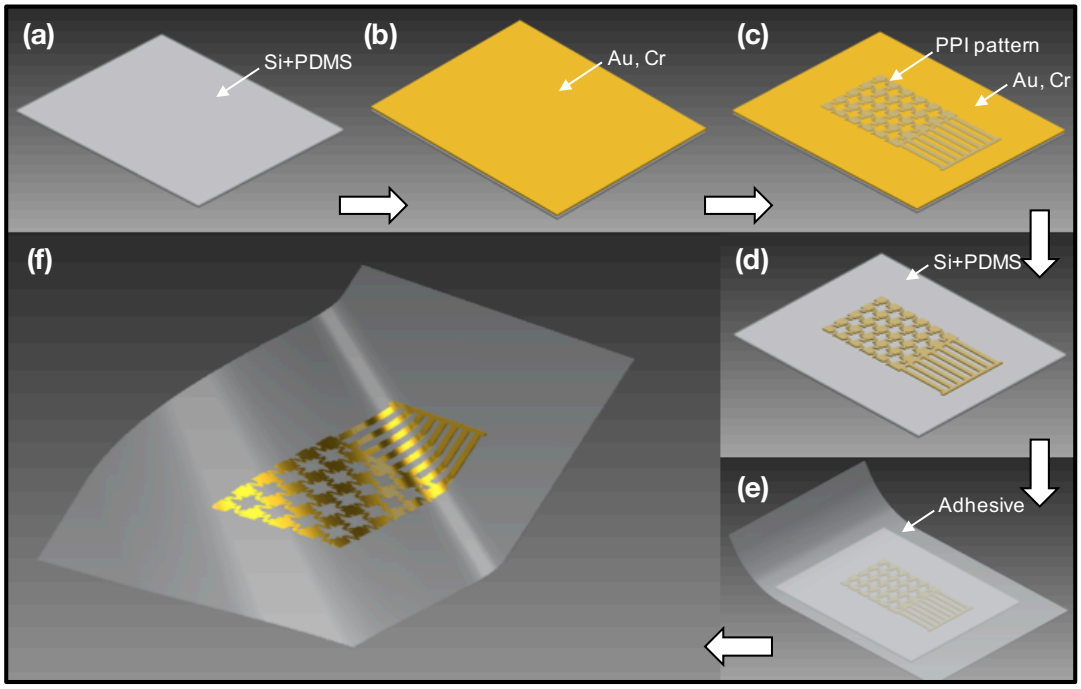

Figure 2.2: Fabrication process for AP sensors **(a)** Formation of weakly-adhering donor; **(b)** Metallization of Au and Cr films, respectively; **(c)** Formation and patterning of PPI polymer backbone; **(d)** Etch-back of Cr and Au films using PPI as etch mask; **(e)** Flexible adhesive substrate adhered to pattern, ready for peel-off; **(f)** Pattern peeled-off onto receiving adhesive with Au surface exposed, ready for use.

2.3.3 EEG & Statistical Testing

To assess the electrophysiological recording capability of new AP sensors, and signal similarity to traditional TP sensors, electroencephalography (EEG) acquisition was performed with both sensors recording side-by-side in a frontal montage. Three subjects were each tested on two separate occasions for eyes-opened and eyes-closed EEG data, acquiring data from both TP and AP sensors. The testing paradigm epoch is as follows: 10s eyes-opened followed by 20s eyes-closed. This process is repeated twice more (90 continuous seconds of EEG data, for a total of 3 epochs) to ensure data without deviant artifacts from the independent recording systems. Of these 3, the cleanest (i.e. least noise prone) epoch is chosen per subject, per trial – this results in a total of $N = 6$ epochs of TP-AP EEG data from 3 subjects. Because both sensor sets are used simultaneously, each epoch consists

of synchronized TP and AP biopotential data. Data sets are then post-processed to yield Pearsons Correlation coefficient values for evaluation of similarity between TP and AP sensor performance.

2.3.4 Peel Testing – Initial Interfacial Characterization

PDMS-sensor interfacial adhesion was characterized by peel tests performed on an array of AP patterns. An array of equally spaced, 1cm x 1cm solid square patterns were fabricated onto a weak-adhering donor substrate as outlined. Peel-off force was measured using a force gauge (M2-2, Mark-1, USA), rigidly coupled to a flat mount lined with adhesive tape. The adhesive end was adhered only to the full $1cm^2$ pattern area and the force gauge pulled upwards, normal to the pattern plane. Maximum force observed during this peel-off was used to characterize the adhesion force between the PDMS-sensor interface. The process was repeated 5 times, at random positions on the donor substrate. Peel force average and variance were calculated using the data.

2.4 Results

2.4.1 Qualitative Comparison of Fabrication Methods for TP and AP Sensors

Figure 2.3 showcases electrical sensors fabricated using the AP process. AP sensors can be densely packed onto the same working area of the donor substrate since submersion in the solvent and wafer dicing are not necessary. Figure 2.3a shows AP sensors on a 4-inch glass wafer, while Figure 2.3b illustrates AP sensors on a Si wafer. The ease with which a sensor can be peeled-off onto an adhesive material (Scotch Tape, 3M, USA) is shown (Figure 2.3c). In contrast, TP sensors are subject to a lengthy release process involving sacrificial layer stripping via solvent treatment, after which a TP sensor carefully undergoes a two-step transfer printing process (sacrificial layer being PMMA, solvent being acetone, and transfer stamp being PDMS). The requirement of controlled pattern release rates from

the donor substrate during sacrificial stripping can often lead to sensors that are deformed from the intended design. These challenges are only magnified when considering larger, more complex heterogeneous sensor patterns, often requiring subjective user judgment and manual dexterity.

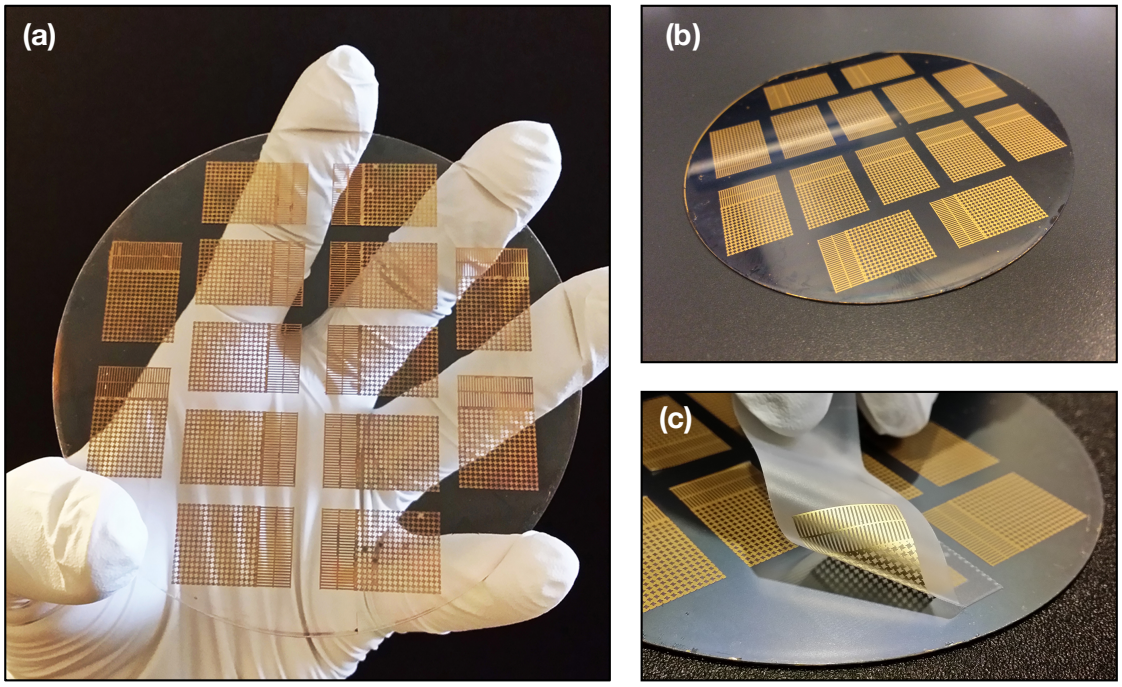

Figure 2.3: Alternative approach AP sensors. **(a)** Dense sensor assembly on rigid glass donor substrate; **(b)** Similar sensor assembly on Si wafer; **(c)** AP sensor peeled-off from Si donor substrate onto adhesive.

Conversely, with the AP approach, the desired pattern is fabricated and objectively post-processed onto a receiving adhesive of choice with a one-step peel-off, obviating the need for solvents and intermediate stamps. The force required to successfully peel-off AP sensors from the weakly-adhering donor was calculated at 0.22 ± 0.03 N. Experimental details can be found in the section 2.3.

A montage of consecutively peeled sensors demonstrates the low variability with which sensors are produced using the AP process (Figure 2.4). Fabricated sensors are accurate to the desired pattern with very little deformity. Although it is possible with the TP approach to retrieve sensors identical to the desired pattern, considerable time and expertise are required if performed manually. Though

automation has been demonstrated for TP production of thin film silicon-based electronics [56–58], these systems require high precision, multi-point calibration, and visual inspection of transfer printing to ensure high yield post-processing. Because the AP approach requires fewer procedures, does not require sacrificial stripping or undercutting, and is not subject to the variability in release rates, there is significant potential for automated post-processing of AP sensors. Comparing both methods, there is an approximately 50% reduction in processing time using the AP method.

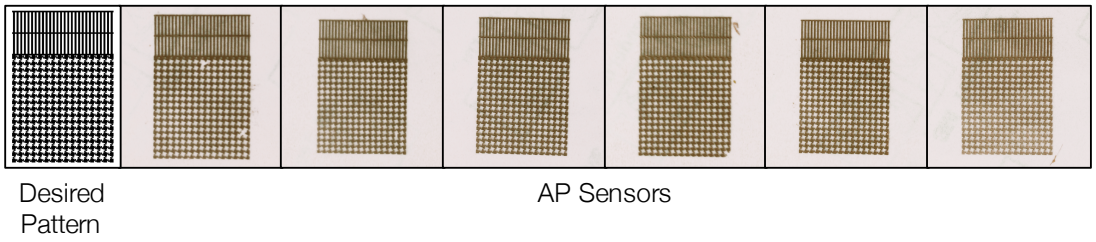

Figure 2.4: AP Sensor variability. Left: desired sensor pattern; Right: AP sensors consecutively peeled-off from same donor substrate. On average, AP sensors closely reflect the desired pattern, primarily because release rates in solvents pertaining to removal of sacrificial layer are not required.

2.4.2 Fabricating on PDMS Surfaces

Microfabrication on PDMS is expected to yield poor adhesion at PDMS-metal interfaces, due to low wettability of PDMS and the large mismatch in thermal expansion coefficients between elastomers like PDMS and thin metal films [59–61]. Consequently, compressive stress develops in thin metal films that induce spontaneous wrinkling and buckling, which can progress to propagating cracks throughout the metal layers [62, 63]. However, there are ways to address the issues of premature buckling of thin Au films during processing on PDMS. During fabrication, we found stiffening of the PDMS-based weakly-adhering layer (by reducing the ratio of PDMS pre-polymer to crosslinker) helped prevent adverse buckling during processing. During sputter-based processing, the known formation of a silica-like layer through plasma exposure prevented the delamination of sputtered AP sensors from their weakly-adhering donor substrates.

Figure 2.5 gives a closer look at the surface topography of peeled-off AP sensors and their respective optimized PDMS surfaces for e-beam evaporated and sputter coated processes. Evaporated sensors appear smooth, exhibiting very little wrinkling (although wafer-length wrinkles occasionally form around patterns during processing); the metal layer shows a regular grain pattern with spherical Au nuclei approximately 50nm in diameter (Figure 2.5a). This smoothness is mirrored by the respective weakly-adhering donor (Figure 2.5b), which maintains a lightly speckled finish akin to the resulting metal grain. In contrast, sputtered AP sensors demonstrate wrinkled surface topography after processing that extends to the underlying PPI backing, and a continuum of elliptical Au particles (Figure 2.5c). The respective PDMS surface maintains the same wavy pattern after the sensor peel-off (Figure 2.5d). This characteristic of Au film wrinkling on PDMS is expected, though wrinkles are not apparent to the naked eye for sputtered sensors. Evaporated sensors, on the other hand, occasionally formed wafer-length wrinkles form around PPI patterns during processing; these wrinkles disappear after PPI development. Despite the differences, both instances of evaporated and sputtered AP sensors maintain their electrical interconnects and sensing properties.

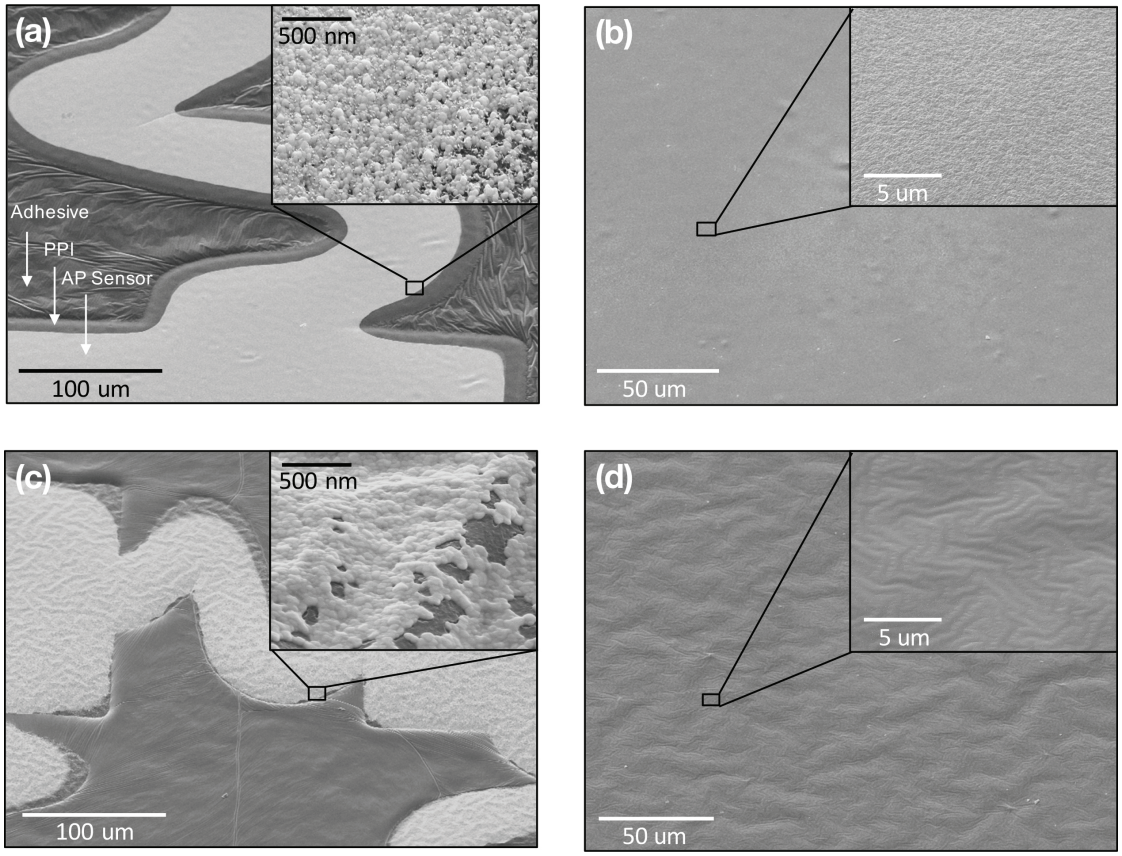

Figure 2.5: SEM images of evaporated and sputter-coated AP sensors. **(a)** Evaporated sensor on adhesive film; **(b)** Weakly-adhering PDMS surface after evaporated sensor peel-off; **(c)** Sputter-coated sensor on adhesive film; **(d)** Weakly-adhering PDMS surface after sputter-coated sensor peel-off; (insets) Zoomed-in surface definition of respective surfaces.

2.4.3 Quantitative Comparison of TP and AP Sensors

To ensure functional characteristics of the sensors are preserved when fabricating with the AP approach, a common eyes-opened/eyes-closed paradigm for measurement of the 8-12 Hz alpha rhythm in electroencephalogram (EEG) [64] was performed. An EEG test was chosen to demonstrate that AP sensors can adequately measure lower amplitude-frequency signals, while indirectly suggesting that larger biopotentials such as ECG and EMG can be easily measured with high fidelity. This is especially true due to golds low impedance in high-frequency bands, as compared to bands characteristic of EEG signals [65,66]. A set of wired

AP and TP sensors on Tegaderm (3M, USA) were connected to semi-encapsulated custom flex cabling (Pica Manufacturing, USA) which is conductive to the sensors, but insulated to the skin. These sets were applied in the 3-lead mastoid configuration, as per Figure 2.6a; each set consisted of recording (REC, forehead), reference (REF, right mastoid process), and ground (GND, left mastoid process) leads. Sensors were carefully arranged side-by-side so to prevent electrical cross-talk between channels (Figure 2.6b, cables not shown). AP and TP sets were wired into an Avatar EEG biopotential amplifier system (Electrical Geodesics, Canada) through the flex cabling. EEG data was simultaneously recorded from both wired sensor sets according to details found in the Materials and Methods section. The acquired biopotential data was sampled at 500 Hz and digitally band-passed in Matlab (MathWorks Inc., USA) to a 6-14 Hz spectral range.

Voltage and time-frequency representations of data from both sensor sets are illustrated in Figure 2.6c-d. Time-frequency plots were generated using the robust spectrotemporal decomposition outlined in the literature [67]. In both representations, the first 10s of data are eyes-opened followed by 20s of eyes-closed data, which is characterized by a 10-12 Hz alpha rhythm (Figure 2.6c,d). Visually, it is easy to confirm that EEG data from both sensor types co-vary closely with one another. This suggests that this alternative microfabrication approach has no significantly negative effect on the acquisition capability of such sensors.

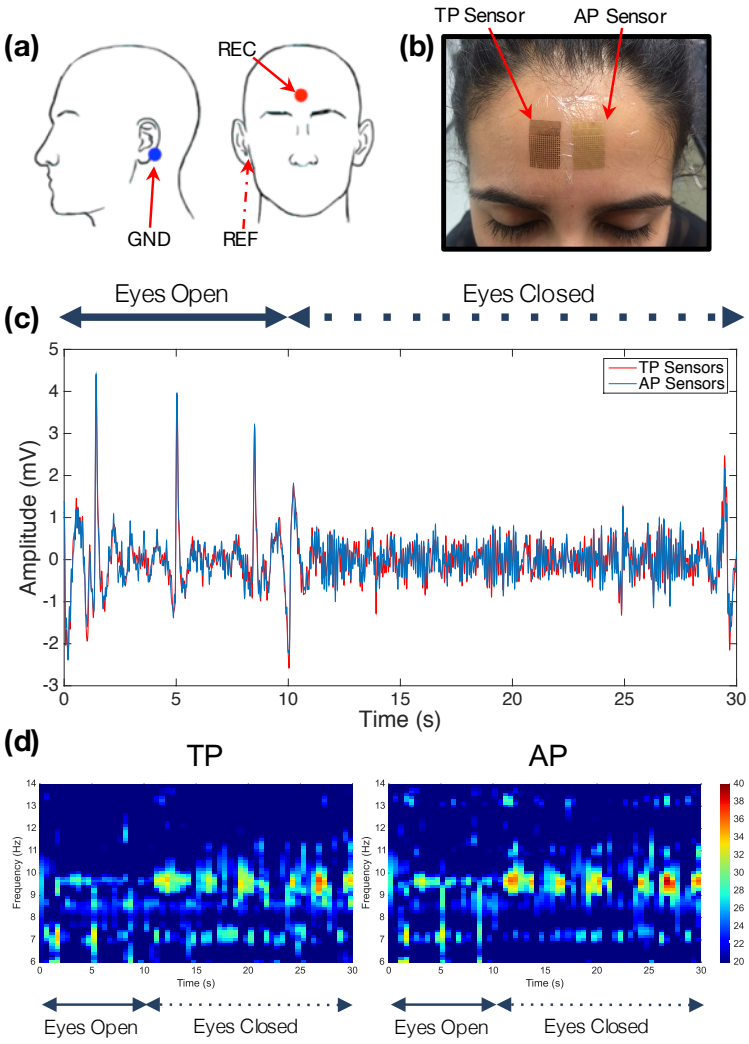

Figure 2.6: Electrophysiological comparison of sensors. **(a)** EEG testing electrode montage; **(b)** Sensors applied to acquisition site — TP on the left, AP on the right; **(c)** Time-Voltage plot for one epoch of data: red = TP, blue = AP; **(d)** Spectrographic representation of epoch: TP on the left, AP on the right. The alpha rhythm begins just after the 10s mark for both sensors.

AP sensor fidelity is compared to that of TP sensors by use of the Pearsons correlation coefficient [68], which ranges from -1 to 1: -1 being negatively correlated, 1 being positively correlated, and 0 representing no correlation.

$$r = \frac{\sum_{i=1}^{n}(X_i - \bar{X})(Y_i - \bar{Y})}{\sqrt{\sum_{i=1}^{n}(X_i - \bar{X})^2}\sqrt{\sum_{i=1}^{n}(Y_i - \bar{Y})^2}} \tag{2.1}$$

Equation 1 is used to calculate the r statistic for each TP-AP pair of simultaneously recorded voltage data. Table 2.1 lists correlation coefficients for each of the 6 TP-AP trials. Many of trials resulted in similar PMMA and AP time series (r >95%), suggestive of AP sensors high fidelity acquisition despite alternative fabrication procedures. Still, perfect correlation is not possible in that both sensors record nuances in thermal noise and motion artifact at the sight of signal acquisition.

Table 2.1: Pearsons correlation coefficients for EEG testing. TP-AP EEG test comparisons across 6 total trials.

Subject	Trial	Correlation Coefficient
1	1	0.95
	2	0.95
2	1	0.98
	2	0.96
3	1	0.95
	2	0.81

2.4.4 Non-Electrical AP Sensors

Using the AP process, other sensor types are easily fabricated for monitoring through other modalities. An instance of this is the production of a variety of simple strain sensors (Figure 2.7a). AP strain sensors are fabricated according to the same framework presented in Figure 2.2; the pattern used during photolithography is replaced by the desired pattern to produce a variety of functional strain sensors with tailored gauge factors. Post-processing of these sensors follows the same peel-off process — from the donor substrate onto the receiving adhesive of choice. The axial strain-resistance performance of one AP strain sensor over several trials is illustrated in Figure 2.7b, and its gauge factor (GF) calculated. With a GF of 0.79, these gold strain sensors demonstrate relatively poor sensitivity to mechanical stimuli, as compared to other strain gauge varieties [69, 70]. However, the emphasis here is that the present method demonstrates versatility in the types

of sensors that can be produced, from which improvements can be made.

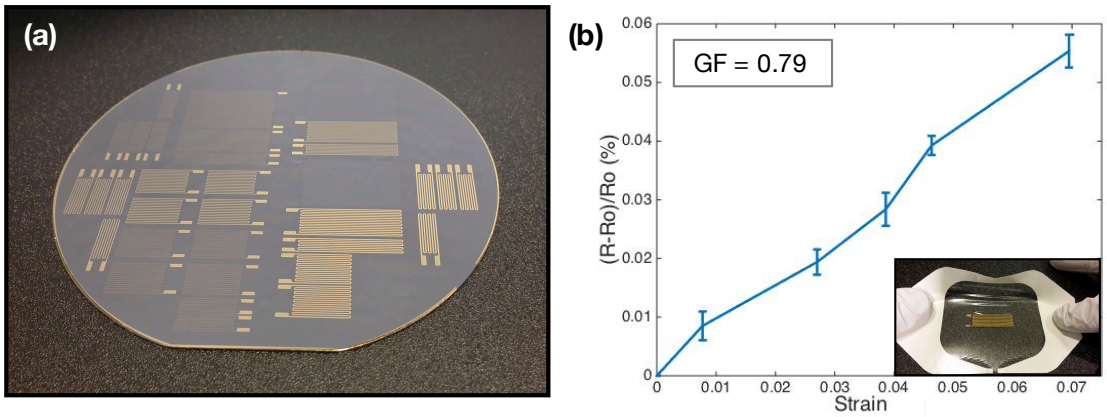

Figure 2.7: Strain sensor fabrication using AP process. **(a)** Strain sensors on wafer; **(b)** Characteristics of AP strain sensors; **(b, inset)** Image of AP strain sensor stretched during testing. Gauge factor (GF) = 0.79.

2.4.5 AP Sensors on Flexible Donor Substrate

Finally, the simple peel-off properties of this method allow us to consider fabrication on flexible donor substrates; this enables the use case of roll-to-roll post-processing. Instead of a silicon or glass wafer, Kapton film was used to fabricate AP sensors; fabrication utilized the same technique outlined (Figure 2.8a,b). AP sensors from flexible donors show no apparent differences as compared to their analogs from rigid donor substrates. To demonstrate their function, a single-channel EKG snapshot acquired using wired AP sensors is shown in Figure 2.8c, clearly illustrating a strong QRS complex alongside P and T waves. One can imagine simply inserting a roll of AP sensors to an existing tape manufacturers production line (with some modifications), where AP sensors are directly peeled directly onto the target adhesive and sent out to the end user.

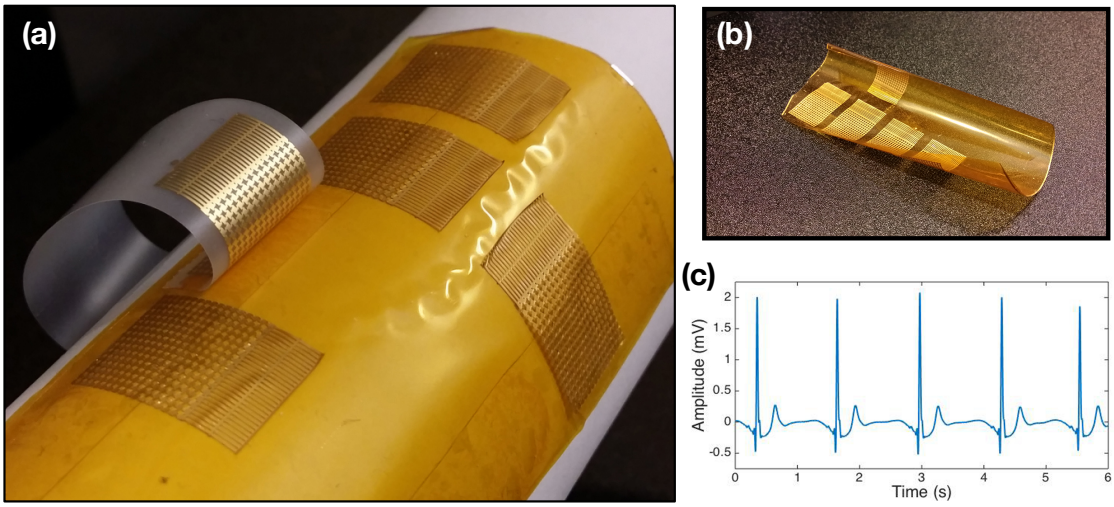

Figure 2.8: AP Sensors processed and peeled-off a flexible donor substrate. **(a)** AP sensors half-peeled by consumer tape with flexible weakly-adhering donor mounted on a tube; **(b)** Free-standing flexible donor substrate with sensors; **(c)** Time-voltage plot of EKG acquired using AP sensors off flex donor.

2.5 Discussion

Here we have presented a process scheme by which a class of flexible sensors can be fabricated and post-processed in a relatively efficient manner. It is important to emphasize here that while there is vast significance in flexible sensor capability and performance, we ultimately require a process that can scale with research and consumer needs. It is mentioned that roll-to-roll processing is a ubiquitously used industrial process, which boasts efficiency at the levels of cost and automation. Rather than re-invent the wheel for accommodating these growing spaces, it is in our interest to leverage the maturity of other processes such as roll-to-roll, at least initially at the stage of post-processing and packaging.

To summarize, our AP sensors are fabricated on a weakly-adhering donor substrate through an inverted construction. Fabrication with PDMS is a not a new concept – previous methods have demonstrated thin film formation and encapsulation of constructs with PDMS featured as the donor during a multi-step transfer printing process or underlying substrate [29–32]. Others have created methods by which a device is either transferred to or is initially constructed on PDMS as a final

receiving substrate [71–73]. In some of these instances, oxidized PDMS exhibits relatively strong adhesive properties when in contact with certain materials – such as SiO2 – that promote silanol hydrogen-bonding [74]. Presented herein, PDMS is used as a donor substrate without any modifications, so to exploit its weak (but sufficient) adhesion to Au films [75] during a one step peel- off process. In concert with the reversed deposition of Au/Cr films and polymer backing, we are allowed to simply peel-off target features, obviating the need for sacrificial layers, immersion in solvents, repetitive transfer steps, and intermediate stamps. Other fabrication details – such as the use of PPI for simultaneous patterning and polymer formation – make for a streamlined process with fewer process failures and better resource allocation during AP sensor preparation.

The use of a PPI polymer backbone is attractive here due to its electrically insulating properties, chemical resistance and thermal stability. Moreover, PPIs known biocompatibility for clinically implantable electronic systems makes it an attractive polymer over conventional photoresists [76]. Because some emphasis is placed on the use of AP sensors for wearable/clinical applications, PPI appears to be the most feasible polymer to implement in the methodology. For sensors not involving biological systems, we speculate other polymers like a photoresist can be used while maintaining the combined formation/patterning step of the AP sensor backbone, though this needs to be investigated.

Ultimately, any adhesive or adhesive-coated material that can effectively adhere to the desired pattern (for the weakly-adhering donor example, with an adhesive force approximately >0.2N) is likely to perform a successful peel-off of AP sensors during post-processing. Moreover, knowledge of the range of forces necessary for successful peel-off enables us to consider situations where one might initially constrain the adhesive to be used and reverse engineer the adhesion force between PDMS and Au films. For example, if certain types of strong adhesives cannot be used due to their damaging of a target surface (e.g. application on neonates with sensitive skin) [77], there is opportunity to tailor the PDMS-sensor interface. In doing so, one can decrease the interface adhesion for facilitating peel-off with weaker adhesive material, while maintaining AP sensor stationarity during

microfabrication.

Because Au flexible sensor fabrication is possible with the weak-interface approach outlined, a next step is to better characterize the interfacial adhesion and exploit this method for use with other interfacing material types. It is known that noble metals possess a proclivity for weak adhesion to an elastomeric rubber such as PDMS [75]. We surmise the methods outlined here can be readily implemented for other metals most similar in nature to Au. Of interest might be metal substitutes such as Ag, of which can be post-processed for yielding Ag/AgCl (one of the best suited for DC coupled signal acquisition) and Pt AP sensors (used for its long-term stability and biocompatibility in vivo; standard practice in neural stimulation) [65,78]. AP sensors comprising Ag or Pt as the interfacing material may be possible to fabricate by simply changing the layer designations during reverse metallization.

Integrated systems of AP sensors with miniaturized back-end transmission and processing circuits may be possible using the present approach. With improved integration of active components and passive interconnections, there is opportunity to integrate with miniaturized rigid electronic circuits [79–81], or further transition away from rigid and stiff electronic assemblies to more flexible and unobtrusive options [28–30]. Advances in this regard might be spurred by recent actions to strengthen the infrastructure of U.S. manufacturing of smart flexible hybrid electronics systems [82].

A degree of Au film micro-scale buckling is observed during sputter-based AP sensor fabrication, though this characteristic of sputtered sensors has not been observed as detrimental to the sensor fidelity. To the naked eye, sputtered metal films on optimized PDMS maintain their adhesion during processing and do not present large wrinkles, buckling, or cracks. It is important to note however that an overall ease with which the sensors can be peeled-off by an adhesive is maintained in spite of this adhesion. We hypothesize that during the sputter coating process, Au nanoparticles are engulfed by the elastic PDMS surface, creating immobilized nucleation sites that resist metal film delamination during processing. Moreover, it appears that sputter coating in this instance is responsible for rendering a wavy PDMS topography as a consequence, surface area is increased which might give

rise to better adhesion. It has been reported that gaseous plasma treatment (e.g. Ar plasma) during sputter coating increases the wettability of PDMS and prevents fast hydrophobic recovery of the PDMS surface, through the creation of hydroxyl-terminated, silica-like surfaces [83–85]. This phenomenon, in concert with the increased surface area and engulfed Au nanoparticles, may explain the unexpected immobilization of Au films during processing on PDMS.

During early evaporation tests, buckling in Au films often lead to propagating cracks, as was expected due to differences in PDMS and Au thermal expansion coefficients. We sought to remedy the buckling issues by addressing the mechanical mismatch between the underlying PDMS and the metal film above. It is known that the relative stiffness of PDMS depends on the ratio of pre-polymer to crosslinker agents used. The result of a smaller ratio is a stiffer PDMS structure that exhibits a relatively large elastic modulus, as compared to lower ratios [86]. Keeping this in mind, stiffer concoctions of PDMS (e.g. 3:1) were used, the idea being that stiffer PDMS (of higher elastic modulus) will resist expansion, therefore reducing the disparity in expansion during thermal cycles. A reduction in film buckling was observed, with no signs of cracking in the resulting AP sensors. Moreover, total film lamination appeared to improve during processing, though this was not quantitatively inspected. Ultimately, evaporated AP sensors maintain their interconnections conductance during processing, and easily peel-off the underlying PDMS surface.

Though the AP approach allows for easy peel-off of microscale thin film features, one should consider the sensor design to be employed. Poorly fashioned sensor patterns and z-thick metal-PPI stacks may result in micro-cracks across stress raisers during the peel-off process. Other pattern characteristics, such as the x-y thickness of pattern features, may pose similar issues due to the inherent tug-of-war between the weakly-adhering donor and receiving adhesive during the peel-off process. We speculate that an increase in effective x-y area will cause a departure in the observed peel-off force threshold, requiring stronger adhesives. Conversely, a decrease in the x-y area might give rise to premature release of patterns during fabrication on the donor substrate, causing problems with device yield. Although

our methodology was successful for relatively large 1cm x 1cm square features, design constraints and peel-off force thresholds should be characterized for better understanding the nature of this weak adhesion and applying relevant findings to future work outlined above.

Lastly, although the present method boasts efficiency over previous works, AP sensors require an adhesive surface for facilitating peel-off. Moreover, AP sensors cannot be re-used, as the necessary adhesive for peel-off wears down during use and is difficult to re-apply. Instead, AP sensors might be immediately suitable as single-use, peel-and-stick sensors in the arena of clinical patient monitoring – where disposable systems are preferred due to concerns of sterility and contamination — and more generally in the spaces of consumer and industrial sensing that benefit from single-use flexible form factors.

2.6 Conclusion

In summary, the work here describes a microfabrication method utilizing unconventional procedures for faster production of ultrathin AP flexible sensors on adhesives. AP sensor production utilizes standard microfabrication procedures while leveraging the expected weak adhesion between PDMS elastomeric substrates and thin Au films. The methodology is agnostic to the different procedures for metallization and robust to adverse cracking of sensor layers. Though sensor performance enhancement is not the aim the present method, sensors are objectively processed and peeled-off onto flexible adhesive substrates in a manner that provides substantial improvements over existing thin film methods. With significant technological advances in the realms of wearable and industrial sensors and circuits, it is important to develop and optimize methods for which production of these technologies is commensurate with their current and projected commercial demands. Keeping pace with these trends and demands will allow us to more readily disseminate flexible electronics technology and usher in a new facade of our everyday devices.

2.7 Acknowledgements

Chapter 2, in full, is a reprint of the material as it appears in *Sensors* 2015. Kang, Dae Y.; Kim, Yun Soung; Ornelas, Gladys; Sinha, Mridu; Naidu, Keerthiga; Coleman, Todd P., MDPI AG, 2015. The dissertation author was the primary investigator and author of this paper.

This research was supported by the National Science Foundation (NSF SMA-1451221), the Bill and Melinda Gates Foundation (GCF-OPP1061388), the Naval Medical Research Center (W911QY-12-C-0090), the Gerber Foundation (GF-554-3288), the National Science Foundation Graduate Research Fellowship (2012137216), the UCSD Institute of Engineering and Medicine Graduate Fellowship, and the NSF-supported San Diego Nanotechnology Infrastructure (SDNI) of UCSD (ECCS-1542148).

Chapter 3

A State Space and Density Estimation Framework for Single-Channel Sleep Staging in Obstructive Sleep Apnea

Chapter 3 presents research findings previously published in Kang, D.Y. et al. 2017 [87]. Here, I delineate my work on a statistical machine learning algorithm, that makes use of state space dynamics to adequately score whole-night sleep architecture using only a single bi-polar channel of sleep EEG. Similarly to Chapter 2, this piece represents a response to the second issue with current sleep monitoring practices, namely the inability to analyze sleep biosignals in an objective and high-throughput manner.

3.1 Abstract

Although the importance of sleep is increasingly recognized, the lack of robust and efficient algorithms hinders scalable sleep assessment in healthy persons and those with sleep disorders. Polysomnography (PSG) and visual/manual scoring remain the gold standard in sleep evaluation, but more efficient/automated

systems are needed. Most previous works have demonstrated algorithms in high agreement with the gold standard in healthy/normal (HN) individuals – not those with sleep disorders. This paper presents a statistical framework that automatically estimates whole-night sleep architecture in patients with obstructive sleep apnea (OSA) – the most common sleep disorder. Single-channel frontal electroencephalography was extracted from 65 HN/OSA sleep studies, and decomposed into 11 spectral features in 60,903 30s sleep epochs. The algorithm leveraged kernel density estimation to generate stage-specific likelihoods, and a 5-state hidden Markov model to estimate per-night sleep architecture. Comparisons to full PSG expert scoring revealed the algorithm was in fair agreement with the gold standard (median Cohens kappa = 0.53). Further analysis revealed modest decreases in median scoring agreement as OSA severity increased from HN (kappa = 0.63) to severe (kappa = 0.47). A separate implementation on HN data from the Physionet Sleep-EDF Database resulted in a median kappa = 0.65, further indicating the algorithms broad applicability. Results of this work indicate the proposed single-channel framework can emulate expert-level scoring of sleep architecture in OSA. Algorithms constructed to more accurately model physiological variability during sleep may help advance automated sleep assessment, for practical and general use in sleep medicine.

3.2 Introduction

Sleep, like eating and breathing, is an essential part of the daily life cycle. Although the process of sleep is not fully understood, it has been shown to play a vital role in immune, cardiovascular, and neurocognitive function [12]. Despite its great importance, nearly 40% of US adults experience problems with sleep ranging from insufficient total sleep time, trouble initiating or maintaining sleep (insomnia), circadian rhythm disorders, sleep-related movement disorders, and sleep-related breathing disorders such as obstructive sleep apnea (OSA) [8]. All of the above have been shown to take a toll on the affected individual physically, mentally, financially, and/or socially.

Sleep disorders can be diagnosed by an overnight polysomnogram (PSG), which utilizes multiple sensing modalities to measure biophysiological signals, including electroencephalogram (EEG), electrooculogram (EOG), and respiratory rate and flow [8]. Although considered the gold standard, there are multiple reasons that hinder more widespread PSG use. First, the cumbersome nature of the equipment interferes with sleep. Second, both the equipment, and the cost/time of a registered polysomnography technician (RPSGT) who performs sleep scoring visually according to standard rules, are expensive. Third, clinical scoring of sleep remains a mundane process with considerable inter-rater variability. To maintain a standard level of clinical sleep scoring, technicians/physicians adhere to rules delineated by Rechtschaffen and Kales (R&K) and the American Academy of Sleep Medicine (AASM), which are designed to visually categorize any epoch of sleep into one of five clinically-recognized sleep stages (Wake, N1, N2, N3, REM) [9, 10, 88]. Despite standardization efforts, the mean inter-rater agreement between experts scoring sleep in OSA is only 71% [14]. [6]. For all these reasons, relatively few sleep studies are performed. A robust, yet cost-effective and minimally invasive system to accurately measure sleep would be valuable to better understand sleep in a research and clinical context.

In an attempt to remedy the problems of manual sleep scoring, many in the literature have proposed machine learning and data science techniques for facilitating automated scoring of sleep. Such studies have employed algorithms such as decision trees [89–93], support vector machines [94–97], Markov models [98–103], and neural networks [104, 105], which operate on combinations of the traditional multi-channel PSG biometrics (e.g. EEG, EOG, Respiration) to provide algorithmic and automated assessment of a patients underlying sleep architecture. To further simplify the current sleep scoring paradigm, many have presented algorithms which perform on very few or even single-channel recordings from varied modalities during sleep. [91, 92, 94, 95, 98, 104–109].

While progress has been made in the multi- and single- channel domain of automated sleep scoring, agreement can be modest – especially when the number of inputs is restricted. Additionally, most of the prior work has focused on sleep

in healthy/normal (HN) subjects. These algorithms may not generalize to older individuals with chronic diseases, or those with sleep disorders that cause sleep fragmentation, such as OSA. Given that 25-50% of middle aged men and women may have clinically relevant OSA [6], algorithms will need to be capable of assessing sleep in a wide range of people. Additionally, to be feasible, data will need to be derived from smaller systems and a minimal number of channels.

Presented herein is an algorithmic approach to scoring sleep using only a single frontal channel of EEG that is satisfactory for automated sleep scoring within the context of OSA. The work assesses time-frequency features of sleep EEG generated via the multitaper spectrogram, and leverages a non-parametric likelihood model for each of the five sleep stages via kernel density estimation. Whole-night sleep architecture is estimated using a five-state hidden Markov model and the Viterbi algorithm, designed to operate on the multimodal likelihood structure of different sleep stages. Results are presented for per- night and per-epoch comparisons of algorithm vs. clinical scoring of the sleep data in subjects who are HN as well as those with OSA. The paper concludes with a discussion of the results and insight into algorithm performance as a function of OSA severity.

3.3 Methodology

The present work includes a retrospective analysis of eighty clinically-scored overnight PSG studies. The analysis was divided into two parts: 1) An analysis of 65 datasets recorded at UC San Diego for 15 HN ($\mathrm{HN_{UCSD}}$) and 50 OSA ($\mathrm{OSA_{UCSD}}$) combined datasets, and 2) an analysis of 15 HN datasets derived from the Physionet Sleep-EDF Database ($\mathrm{HN_{Physionet}}$) [110, 111].

The first sixty-five datasets were recorded on a 1401-plus interface and Spike 2 software (Cambridge Electronic Design Ltd., Cambridge, UK) at the UCSD Sleep Laboratory in San Diego, California. Ethical approval for these studies was obtained from the Human Research Protections Program at the University of California, San Diego. Manual scoring of sleep was performed by a RPSGT who had access to all modalities included in the full PSG study to create the clinical

hypnogram. Fifty of the sixty-five UCSD datasets – comprising a subtotal of 48,819 30s epochs of sleep – contained a mix of OSA severities based on the Apnea Hypopnea Index (AHI); 9 were mild OSA ($5 \leq$ AHI < 15/hour), 9 were moderate OSA ($15 \leq$ AHI < 30/hour), and 32 were severe OSA (AHI ≥ 30/hour). Another fifteen of the sixty-five datasets – comprising a subtotal of 12,084 30s epochs of sleep – contained HN data (AHI < 5/hour). A total of 60,903 30s epochs were used in the five-fold cross validation scoring analysis described below.

For the purposes of this study, only a single EEG channel (F3-A2) and the clinical hypnogram from the full HN_{UCSD} and OSA_{UCSD} PSG studies were used for training and testing of the automated algorithm. Figure 3.1 illustrates the process workflow for automated assessment of sleep via single-channel sleep EEG. The algorithm classifies a continuous sleep EEG signal into a 5-stage sleep paradigm comprised of stages Wake (W), REM (R), N1, N2, and N3. Python 3.4.4 and modified scripts from of the scikit-learn library were used to create the algorithm.

The final fifteen of eighty datasets were derived from the public Sleep-EDF Database [110, 111]. Specifically, EEG channel Fpz-Cz and clinical hypnograms were extracted from Sleep Telemetry subjects 01-02, 04-14, and 16-17. All recordings were obtained from subjects who had mild difficulty falling asleep, but who were otherwise healthy. Processing of these datasets followed suit with the HN_{UCSD} and OSA_{UCSD} data. Sleep architecture estimation of the $\text{HN}_{\text{Physionet}}$ sleep EEG datasets was performed: 1) as a training-testing analysis entirely separate from the UCSD-trained algorithm, and 2) by treating the $\text{HN}_{\text{Physionet}}$ data as test data against the UCSD-trained algorithm. The former assessed the generalizability of the raw algorithm, while the latter assessed generalizability of the F3-A2 training for classification of data derived from other EEG montages.

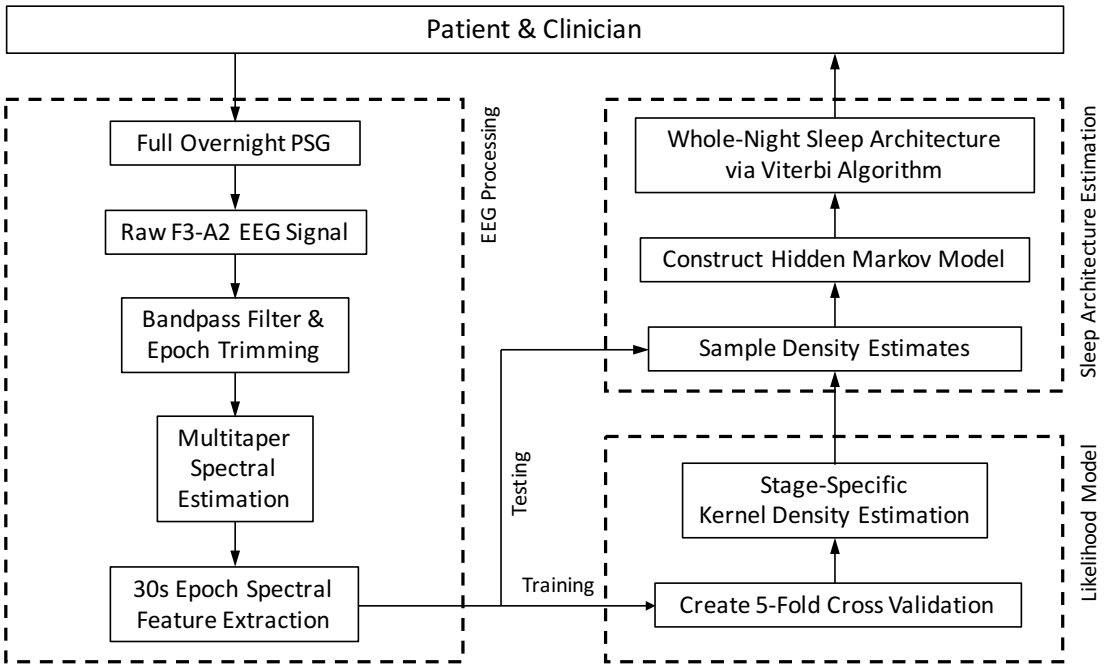

Figure 3.1: Process workflow for automated assessment of single-channel sleep EEG.

3.3.1 EEG Pre-Processing

Raw single channel F3-A2 EEG data were derived from full PSG recordings in each of the 65 UCSD datasets. Single-channel EEG was originally sampled at 125Hz. Time series EEG data was bandpass filtered between 0.1Hz and 50Hz using a zero-phase forward-backward filter (Python, SciPy module). After filtering, 30s epochs of sleep deemed as NO STAGE in the clinical hypnogram were trimmed from both the hypnogram and at corresponding points in the time series EEG data. NO STAGE epochs only appeared at the beginning or end of clinical hypnograms (accounting for subject wiring and disconnection during the overnight PSG), so EEG signal continuity during epoch trimming was preserved.

Similarly, raw single channel Fpz-Cz EEG data were derived from each of the 15 Physionet datasets. Single-channel EEG was originally sampled at 100Hz. The first 6-hours of each $HN_{Physionet}$ dataset was used, to ensure alignment between the EEG data and corresponding hypnograms. In these hypnograms, epochs Stage 3 and Stage 4 were replaced by N3, to be consistent with the analysis of UCSD

data.

3.3.2 Multitaper Spectral Estimation

Filtered EEG signals were spectrally decomposed using multitaper (MT) spectral estimation. Like the conventional fast Fourier transform (FFT), MT spectral estimation is an approach for constructing a time-frequency representation of non- stationary time series signal. The advantage in using the MT approach is in its use of orthonormal bases to serve as different, uncorrelated tapers (hence multitaper), resulting in a modulation of spectral estimation variance and bias [112–114]. MT spectral estimation also boasts better frequency resolution than some overlapping segment average approaches, such as Welchs method, for the same spectral leakage and variance estimators; specifically, the resolution bandwidth for Welchs method is 20-60% wider than the MT approach [115].

In essence, these multiple tapers are auxiliary to the standard FFT – each taper augments the FFT separately; the outputs of which are averaged across the total number of tapers used to assemble the MT spectral estimate (1, 2). If $x(n)$ is the time series acquisition of sleep EEG with discrete samples $n = 0, 1, ..., N, \Delta$ represents the time interval between recorded samples, and $h_n^{(i)}$ denotes the set of orthonormal tapers $i = 1, 2, ..., L$ at each time sample n, then the MT power spectral density (PSD) estimate of the sleep EEG signal, S, was given by

$$S(f) = \frac{1}{L} \sum_{i=1}^{L} S^{(i)}(f) \tag{3.1}$$

where

$$S^{(i)}(f) = \Delta | \sum_{t=0}^{N-1} h_n^{(i)} x_n e^{-i2\pi t f \Delta} |^2 \tag{3.2}$$

For a mathematical narrative on MT spectral estimation, Babadi and Brown provide a brief derivation of the MT method and a comparison to other non-parametric spectral estimation techniques [113]. In the proposed algorithm, EEG MT spectral estimation was implemented in Python via the Spectrum module available in the Python Package Index. A 30s non- overlapping window and a

suggested time half-bandwidth parameter $NW = 3$ were used, which resulted in $L = (NW)(2) - 1 = 5$ tapers used for EEG MT spectral estimation. Discrete prolate spheroidal sequences – or Slepian sequences – were used as the orthonormal set of tapers. Finally, was converted to a log-PSD:

$$y_t(f) = 20 * log_{10} S(f) \tag{3.3}$$

3.3.3 EEG Spectral Feature Extraction

Eleven spectral features were extracted on an epoch-by-epoch basis from the log-MT spectral estimate of sleep EEG (Table 3.1). Frequency bands were chosen based on the previous literature and guidance from the AASM Sleep Scoring Manual [10, 88, 96, 102, 103, 105].

Table 3.1: Spectral Features used for automated classification of sleep EEG.

EEG Frequency Bands/Features	*Spectral Edges (Hz)*	*Characteristic Sleep Stage*
*Broadband (**broad**)*	(0.1, 50)	W (Motion Artifact)
*Gamma (**γ**)*	(30,50)	W
*Beta (**β**)*	(20, 30)	W
*Sigma (**σ**)*	(11, 14)	N2 (Sleep Spindles)
Alpha ($\alpha_1, \alpha_2, \alpha_3, \alpha_4$)	(7, 8), (8, 9), (9, 10), (10, 11)	W, N1, R
*Theta (**θ**)*	(4, 7)	N1, R (Sawtooth Waves)
*Delta (**δ**)*	(1, 4)	N3 (Slow Waves)
*Very-Low Frequency (**vlf**)*	(0.1, 1)	W (Eye Blinks), R (Rapid Eye Movements), N2 (K-Complexes)

Of interest here was the decision to split the 7-11Hz alpha band into four equally spaced bands of 1Hz bandwidth. This was done to implement insight from the AASM Scoring Manual, which states, *The alpha frequency in stage R often is 1-2Hz slower than during wakefulness.* [88] Moreover, stages R and N1 often resemble each other in low-amplitude, mixed frequency activity. Therefore, a segmentation of the alpha band was performed in an attempt to better discern these three often misclassified stages.

In this work, the spectral feature y_t^k represented a mean PSD value for frequency band k during epoch of an overnight sleep EEG dataset. Denote the set of frequencies in frequency band k as $\mathcal{F}^{(k)}$ and the size of $\mathcal{F}^{(k)}$ as $|\mathcal{F}^{(k)}|$. For instance, for $k = 0$, the *broad* feature, we have that $\mathcal{F}^{(0)} = \{0.1, 0.13, 0.16, ..., 49.96, 49.99\}$ and $|\mathcal{F}^{(0)}| = 1663$. For $k = 1, 2, ..., 10$, the frequency bands pertaining to $\mathcal{F}^{(k)}$ are given in Table 3.1. For $k = 0, 1, ..., 10$, each spectral feature y_t^k calculated as follows:

$$y_t^k = \begin{cases} \frac{1}{|\mathcal{F}^{(k)}|} \sum_{f \in \mathcal{F}^{(k)}} y_t(f), k = 0 \\ \frac{1}{|\mathcal{F}^{(k)}|} \sum_{f \in \mathcal{F}^{(k)}} (y_t(f) - y_t^0), k = 1, 2, ..., 10 \end{cases} \tag{3.4}$$

One feature ($k = 0$, broadband EEG activity) was simply calculated as the mean PSD value between spectral edges (0.1Hz, 50Hz). The remaining features were calculated as relative spectral values – the difference between activity y_t^k in frequency band k (for $k \neq 0$) and broadband activity y_t^0. The result is a feature vector $\mathbf{y_t} \in \mathcal{R}^{11}$ for each 30s clinically-scored epoch of sleep. Over the entire UCSD dataset of 65 overnight studies, a total of 60,903 feature vectors were extracted. For Physionet data, a total of 10,800 feature vectors were extracted.

3.3.4 Kernel Density Estimation

Following epoch-by-epoch spectral feature extraction, the 65 nights of UCSD EEG feature vectors were equally segmented into five separate folds (13 nights per fold: 3 HN_{UCSD} and 10 OSA_{UCSD}), defining the 5-fold cross validation paradigm for algorithm training and testing. Separately, the 15 nights of Physionet EEG feature vectors were equally segmented into five separate folds (3 $\text{HN}_{\text{Physionet}}$ datasets per fold). To construct likelihood models for the feature vector , kernel density estimation (KDE) was used to estimate the conditional probability density function of observing EEG spectral features during a specific stage of sleep.

KDE is a non-parametric method for estimating the probability density function of a continuous random variable. In this formulation, we treat $\mathbf{y}_t^{(i)} = (\mathbf{y}_0^{(i)}, \mathbf{y}_1^{(i)}, ..., \mathbf{y}_T^{(i)})$ as sample vectors of dimension $d = 11$, drawn from the ith

class of an unknown density function $f_Y^{(i)}(\mathbf{y})$. Generally speaking, it is difficult to determine the true distribution $f_Y^{(i)}(\mathbf{y})$, so the following kernel density estimate is used for approximation:

$$R_i(\mathbf{y}) = \hat{f}_{i,b_i}(\mathbf{y}) = \frac{1}{T_i b_i} \sum_{t=1}^{T_i} K\left(\frac{\mathbf{y} - \mathbf{y}_t^{(i)}}{b_i}\right) \tag{3.5}$$

where K is the kernel function – a d-dimensional, non-negative, zero-mean function that integrates to one – and b_i is a non- negative, non-zero bandwidth parameter corresponding to the ith class.

KDE is an attractive means to approximate the true topology of a density. Its formulation is similar to that of a histogram of the data, except that it performs a weighted average of many kernel functions centered about each data point in the sample space. In this way, $R_i(\mathbf{y})$ leverages properties of the chosen kernel K to enforce smoothness and continuity on the likelihood surface.

Moreover, unlike the multivariate Gaussian distribution, $R_i(\mathbf{y})$ can exhibit multimodal behavior, which is necessary for encoding the variations in sleep architecture within and across different patients, pathologies, and nights of sleep. For example, the same stage of sleep could display variants of sleep EEG activity based on age, sex, mental state, and overall health [116]. Inter-individual variability in sleep and frequency of sleep arousals increases as a function of age [117, 118], and is prominent in diseases such as Parkinsons Disease [119] and Rheumatoid Arthritis [120]. Moreover, such variations in regard to sleep arousals and sleep continuity are mitigated by non-anatomical features such as the arousal threshold, which is considered an important contributor to the pathogenesis of sleep breathing disorders such as OSA [121]. By utilizing a density estimation approach, such as KDE, the goal is to model appropriately the heterogeneity of sleep EEG activity within each stage of sleep for varied classes of subjects and sleep physiology.

To construct the trained likelihood models for each sleep stage class, KDE was implemented using the SciPy stats.gaussian_kde package. An 11-dimensional $\mathcal{N}(0, 1)$ Gaussian was used as the kernel function, and the optimal bandwidth parameter — was automatically determined for each sleep stage $i \in \{W, R, N1, N2,$

$N3\}$ via Scotts Rule [122]. For an arbitrary fold of test data, $R_i(\mathbf{y})$ was constructed with the remaining 4 folds of data, so to train the likelihood models with data separate from the testing set. The result per-fold is a set of stage-specific conditional probability density functions $f_{\mathbf{Y}|X}(\mathbf{y}|x)$, where the sleep stage x probabilistically exhibits EEG spectral activity $\mathbf{y}$.

3.3.5 Hidden Markov Model

During each 30s epoch of sleep, a hidden stage of sleep emits observable multivariate EEG spectral activity, giving an indication of the underlying sleep state. The observed EEG signal varies for different stages of sleep, as well as for different nights of sleep and sleep pathologies. As sleep evolves over the course of the night, discrete sleep stage transitions occur between neighboring epochs, constrained by time-varying physiological phenomena governing the sleep process. These transitions are traditionally scored such that *only* the previous epoch can influence the transition to another sleep stage in the current epoch [88]. To encompass these properties of sleep and sleep scoring, a state space model was utilized to represent per-night sleep architecture as a 5-state, transition-constrained, Markov chain. The likelihood model from section 3.3.4 and the Markov model jointly comprise a hidden Markov model (HMM) [123].

To construct sleep architecture as a HMM, the following variables and parameters are defined for epochs $t = 0, 1, ..., T$, and sleep states $i, j \in \{W, R, N1, N2, N3\}$:

$\mathbf{y}_t$: Multivariate observation vector of single-channel EEG spectral feature at time t.

x_t: Hidden sleep state i at epoch t.

$\mathbf{y}_{0:T}$: $(\mathbf{y}_0, \mathbf{y}_1, ..., \mathbf{y}_{T-1}, \mathbf{y}_T)$. Sequence of observed multivariate EEG spectral activity.

$\mathbf{x}_{0:T}$: $(x_0, x_1, ..., x_{T-1}, x_T)$. Sequence of hidden sleep states composing whole-night sleep architecture.

π_i**:** $P(x_0 = i)$. Initial probability of sleep state i at time $t = 0$.

$Q_{i,j}$**:** $P(X_t = j|X_{t-1} = i)$. Probability of transitioning to state j at time t from state i at time $t - 1$.

$R_i(\mathbf{y})$**:** $P(\mathbf{Y}_t = \mathbf{y}_t|X_t = i)$. Probability of observing EEG features $\mathbf{y}_t$ in sleep state i.

The goal is to generate a model for which $\mathbf{x}_{0:T}$ can be estimated through a corresponding sequence of observed EEG activity and prior knowledge of sleep stage transitioning constraints.

The HMM algorithm presented here was formulated using a modified version of the framework available in the hmmlearn python module. The modifications allowed for the use of alternative likelihood models, which are framed as the set of stage-specific KDE likelihoods $R_i(\mathbf{y})$ generated during the training phase. Since all PSG studies begin before the onset of sleep, the only non-zero initial probability corresponds to the sleep state $i = W$, such that the initial probability vector $\pi_i = [1, 0, 0, 0, 0]$. Values from the work of [124] provide insight on the transition properties of sleep in clinical populations of healthy subjects and OSA subjects. As the work was performed for a 4-stage sleep model, OSA-specific values were extrapolated to create a 5-state transition probability matrix for nights of sleep in OSA subjects; transition probabilities are graphically illustrated in Figure 3.2. These values are fixed for each night of sleep in the analysis.

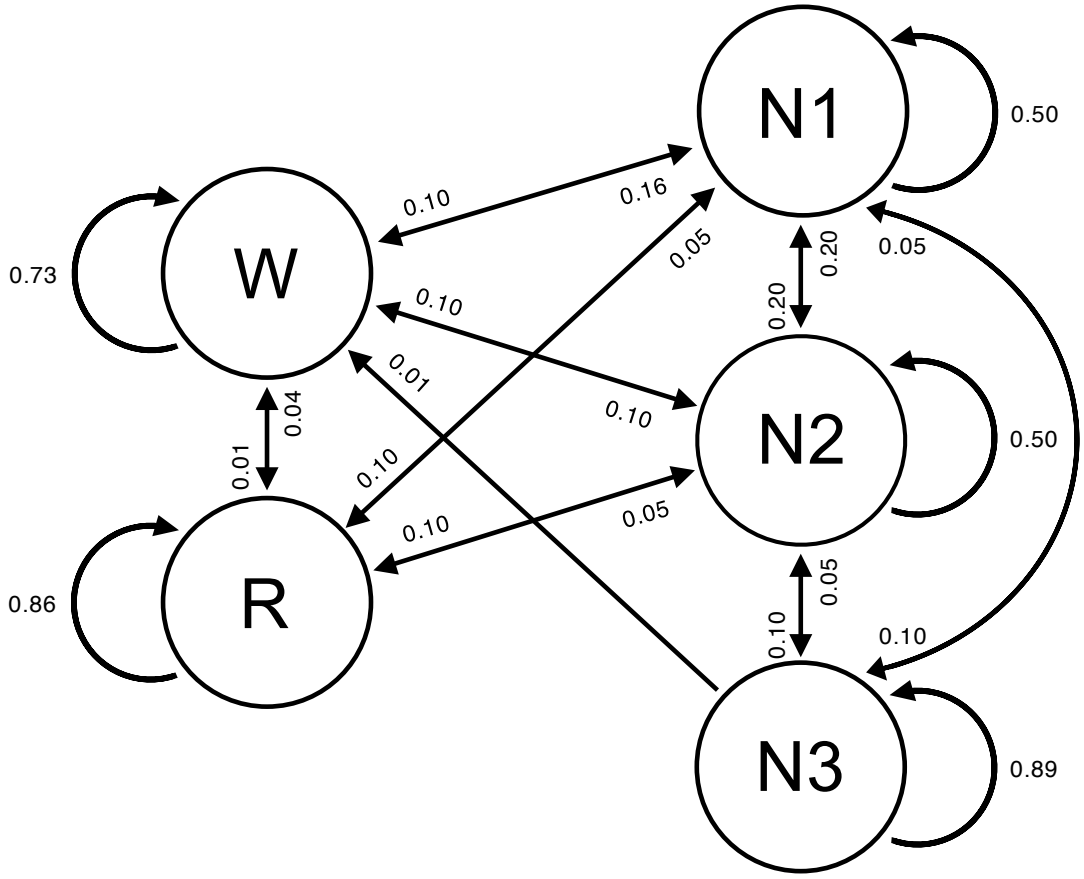

Figure 3.2: Graphical model of HMM sleep state transitions with corresponding probabilities. Absence of directed arrow indicates a transition probability $Q_{i,j} = 0.00$.

Following the HMM formulation, the Viterbi algorithm (VA) was used to generate an algorithmic representation of the 5-state clinical hypnogram. The VA is a recursive decoding method for determining the sequence of latent (hidden) variables most likely associated with a corresponding sequence of observations [123]. In the case of sleep staging, the VA uses the HMM to identify an optimal sequence of hidden sleep stages $\mathbf{x}_{0:T}$ that best fit the observed set of EEG signals $\mathbf{y}_{0:T}$ during a whole night of sleep via maximum a posteriori sequence estimation. The final output is the Viterbi path – a sequence of values $\mathbf{x}_{0:T} = x_0, x_1, .., x_T$ that represents the automated sleep staging for a single night of sleep. This process is performed on a per-night basis.

3.3.6 Comparison to Clinical Hypnogram

To assess the accuracy of the described algorithm, agreement between automated sleep scoring and clinical sleep scoring was determined via Cohens kappa. Cohens kappa (κ) measures the inter-rater agreement between two scorers that classify items into a number of mutually exclusive categories [125]:

$$\kappa = \frac{p_o - p_c}{1 - p_c} \tag{3.6}$$

Here, p_o is the observed probability of agreement between scorers and is the probability of agreement due to chance. In this case, κ is thought to be a more robust measure than raw accuracy. A κ value of 0-0.2 is considered essentially no agreement, 0.2-0.4 slight agreement, 0.4-0.6 fair agreement, 0.6-0.8 high agreement and 0.8-1.0 nearly perfect agreement [126].

3.4 Results

3.4.1 Whole-Night EEG Multitaper Decomposition

To perform automated classification of whole-night sleep architecture, F3-A2 single-channel sleep EEG was spectrally decomposed via the conventional FFT spectrogram and MT spectral estimate.

Figure 3.3 illustrates an example of time-frequency outputs of both methods for 30s, non-overlapping windows over a whole night of sleep. The corresponding manually-scored hypnogram is aligned with both representations of the single-channel EEG data, revealing the connection between EEG spectral features and full PSG-based sleep scored architecture. Conventional spectral decomposition of the sleep EEG signal visually exhibited noisier outputs, as compared to the MT approach. Specifically, spectral bleeding was prevalent in frequency bands between 3-7Hz (i.e. θ and δ waves) and higher frequency components (β and γ) when using the FFT. This is significant since β and γ waves are essential in distinguishing between sleep stages W, R, and N1, as previously noted. Though the MT approach resolved this problem and provided a more de-noised time-frequency image of sleep

EEG, both methods provided clear association between spectral EEG features and manually-scored sleep architecture.

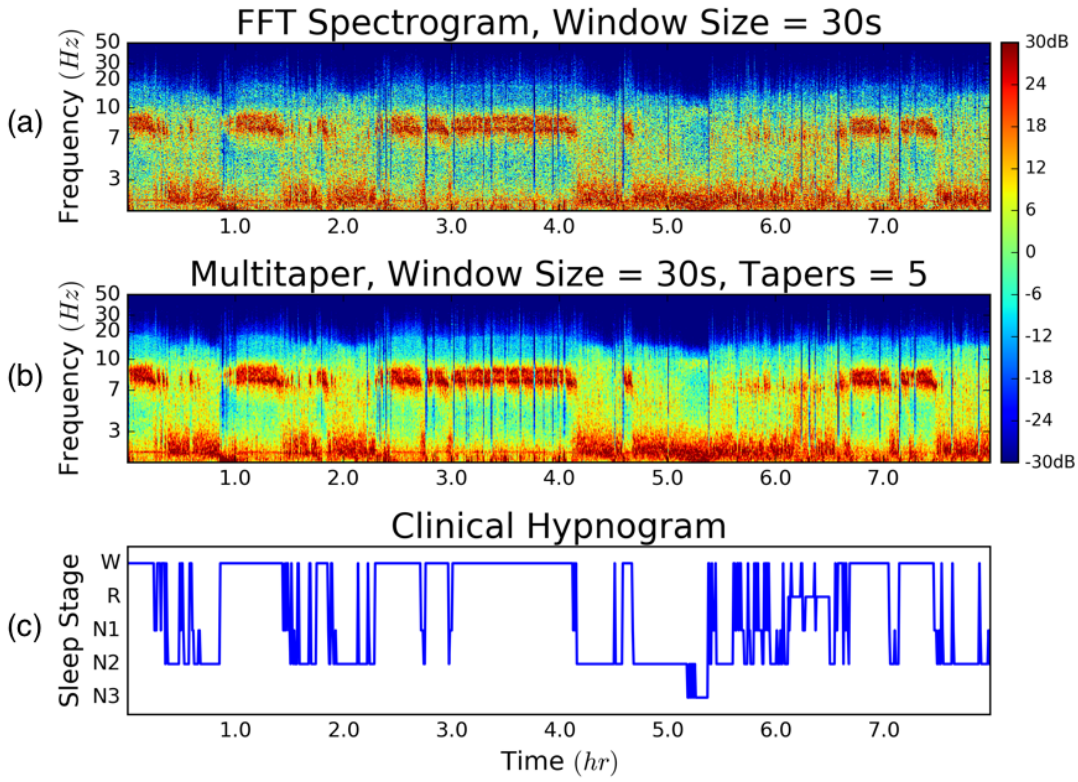

Figure 3.3: **(a)** Conventional FFT spectrogram of channel F3 EEG data for a full night of sleep; 30s, 0s-overlapping windows. **(b)** Multitaper spectral estimate of the same data set; 30s windows and 5 tapers. **(c)** Ground Truth – full PSG, manually-scored clinical hypnogram; 30s epochs.

3.4.2 Sleep Stage Spectral Density Estimation

Following EEG spectral feature extraction, the 5-fold cross validation for 65 nights of HN_{UCSD} and OSA_{UCSD} sleep was constructed. Density estimation was implemented in the training phase of the proposed algorithm to construct the stage- specific EEG likelihood models $R_i(\mathbf{y})$. All 11 features were used for density estimation, culminating in 5 probability density functions specific to W, R, N1, N2, and N3 for each fold of data.

Figure 3.4 illustrates ground truth univariate histograms of all 60,903 extracted spectral features per each sleep stage (55 histograms total). Many EEG

features exhibit bimodal structure within the same sleep stage, supporting the need to go beyond multivariate Gaussian modeling of intra-stage sleep EEG activity. Conversely, Figure 3.5 illustrates histograms for 12,084 epochs of $\mathrm{HN}_{\mathrm{UCSD}}$ data only, revealing unimodal Gaussian-like structure across all sleep stage-EEG feature combinations. Figure 3.6 illustrates an example of the 3D likelihood surfaces of both density estimation and fitted multivariate Gaussian approaches for the domain of γ and *broad* EEG spectral features. EEG spectral data were first used to construct a ground truth histogram of the likelihood surface during stage R (yellow bars). Similarly, the data were used in density estimation to generate a likelihood surface (blue), which closely followed the histograms intricate trimodal structure. Conversely, the fitted Gaussian likelihood surface (red) failed to depict accurately the underlying distribution of γ and *broad* features, instead modeling it as a single wide peak between the three true modes.

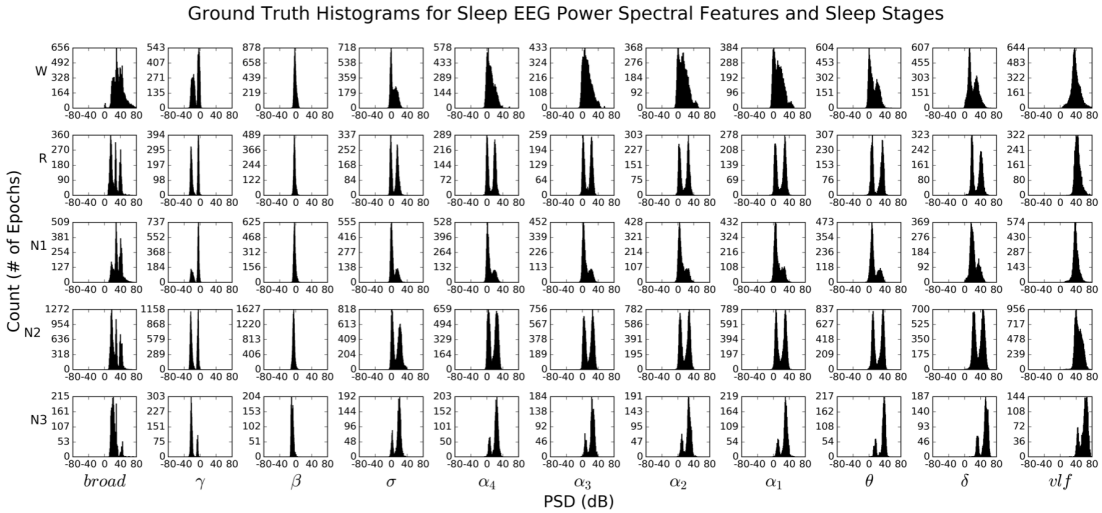

Figure 3.4: Univariate, multimodal histograms of the eleven extracted EEG spectral features listed in Table 3.1, for each true stage of sleep (55 histograms total). Distributions were generated using all 60,903 30s epochs from 65 total HN/OSA datasets and their true corresponding labels from expert scoring. Per-stage breakdown of all labeled 30s epochs: W = 14,582, R = 7,105, N1 = 11,398, N2 = 23,021, N3 = 3,797.

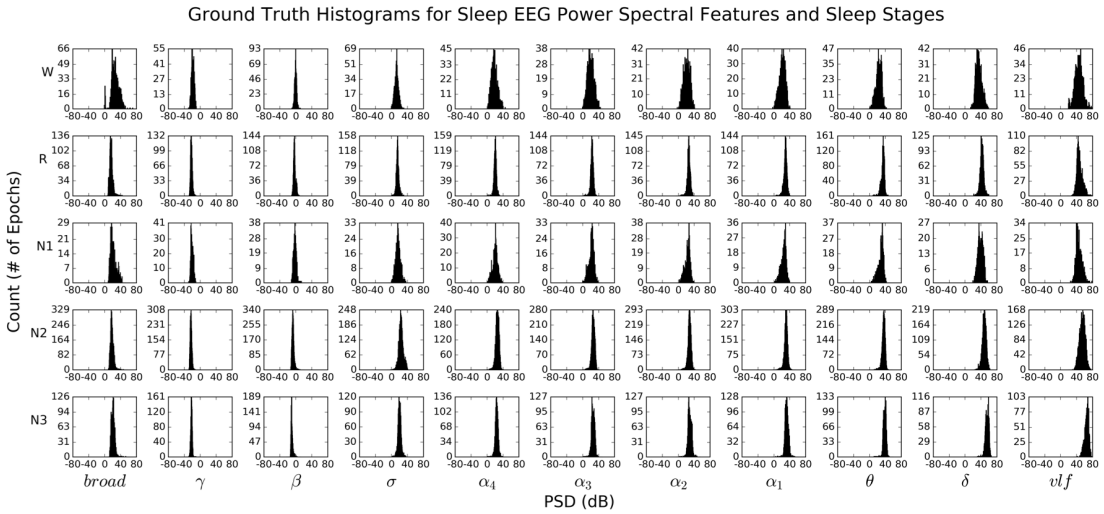

Figure 3.5: Univariate, multimodal histograms of the eleven extracted EEG spectral features listed in Table 3.1, for each true stage of sleep (55 histograms total). Distributions were generated using all 12,084 30s epochs from the 15 HN datasets and their true corresponding labels from expert scoring. Per-stage breakdown of all labeled 30s epochs: W = 1,247, R = 2,351, N1 = 721, N2 = 5,609, N3 = 2,156.

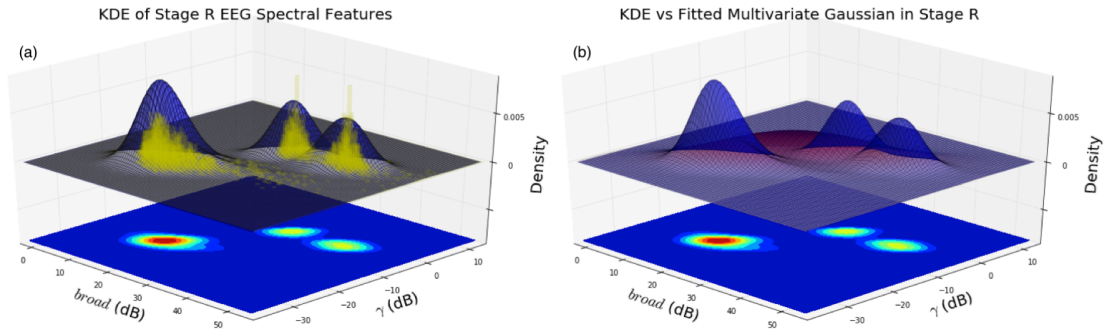

Figure 3.6: **(a)** Yellow = Ground truth histogram of and spectral data in stage R. Blue = bivariate, multimodal distribution of the log-power data generated via density estimation. **(b)** Blue = bivariate, multimodal distribution of the log-power data generated via density estimation. Red = bivariate, unimodal distribution of the same data generated via fitted Gaussian. Floor projections depict the blue estimated surface topography.

3.4.3 Whole-Night Sleep Architecture Estimation

Results from stage-specific density estimation were implemented into the 5-state HMM, along with initial probabilities π_i, transition probabilities $Q_{i,j}$, and testing feature vectors $\mathbf{y}_t$. In concert with the VA, the result was an estimation of whole-night sleep architecture derived from single-channel F3-A2 and Fpz-Cz EEG.

An example of the final algorithmic output is shown in Figure 3.7. The same expert-scored clinical hypnogram from Figure 3.3 is shown again here, juxtaposed with the corresponding automated score. As is evident, the algorithm was able to follow closely the macrostructure of expert-scored sleep architecture despite using only a single channel of EEG. The algorithm was also able to capture many nuances in sleep microstructure such as the many arousals from stage N2 to stage W, and reversions back to sleep. An exception of this was the algorithm under-scoring of stage N2 epochs, which were scored instead as N3 at moments throughout the night of sleep. For this particular night of sleep, the subject had an AHI = 63.1 events/hr, i.e. severe OSA. In spite of this finding, the algorithm was able to score accurately whole-night sleep architecture with a $\kappa = 0.70$. To put this into perspective, the mean inter-rater κ between two experts scoring OSA sleep using full PSG is 0.59 [14].

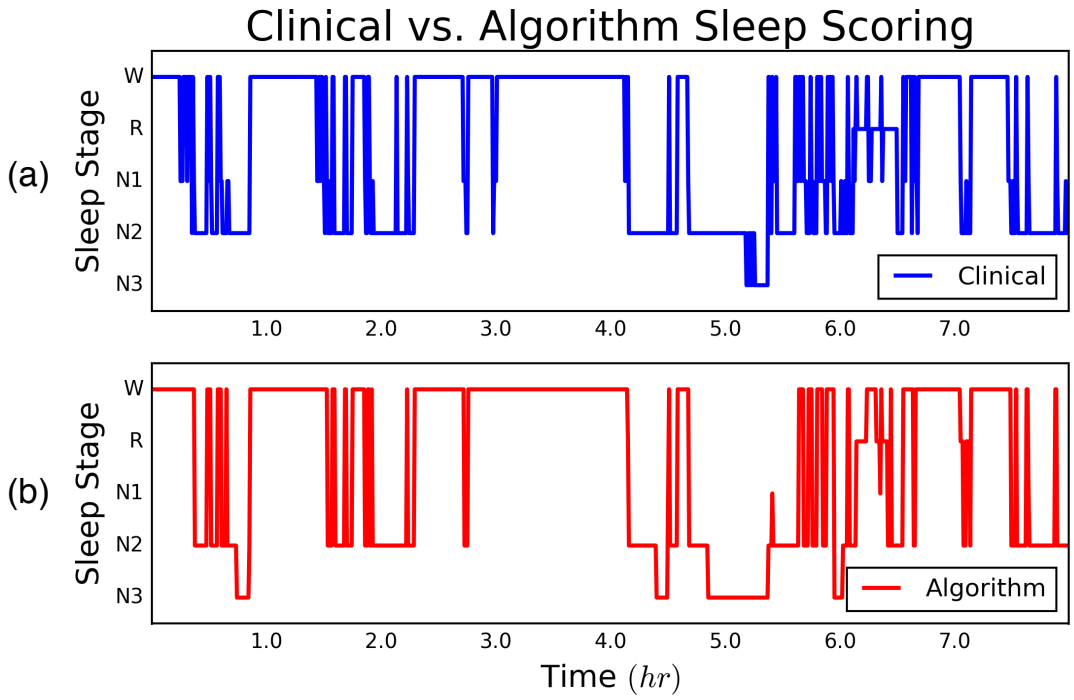

Figure 3.7: **(a)** Clinical Sleep hypnogram from full PSG and technician manual scoring. **(b)** HMM-based Algorithm using single-lead forehead EEG. Subject AHI = 63.1 events/hr; $\kappa = 0.70$.

3.4.4 Per-Night & Per-Epoch Sleep Staging Comparison

Cohens kappa was used to investigate the algorithms per-night classification performance against corresponding expert-scored hypnograms. Furthermore, two instantiations of the proposed algorithm – one using a fitted multivariate Gaussian likelihood model and another using KDE – were employed to investigate the utility of density estimation in modeling the expected multimodal structure of sleep EEG. Figure 3.8 shows a box plot of the per-night κ values generated for each of the two likelihood models. Each model made use of all 65 whole-night UCSD datasets (HN_{UCSD} and OSA_{UCSD}) originally separated in the 5-fold cross validation.

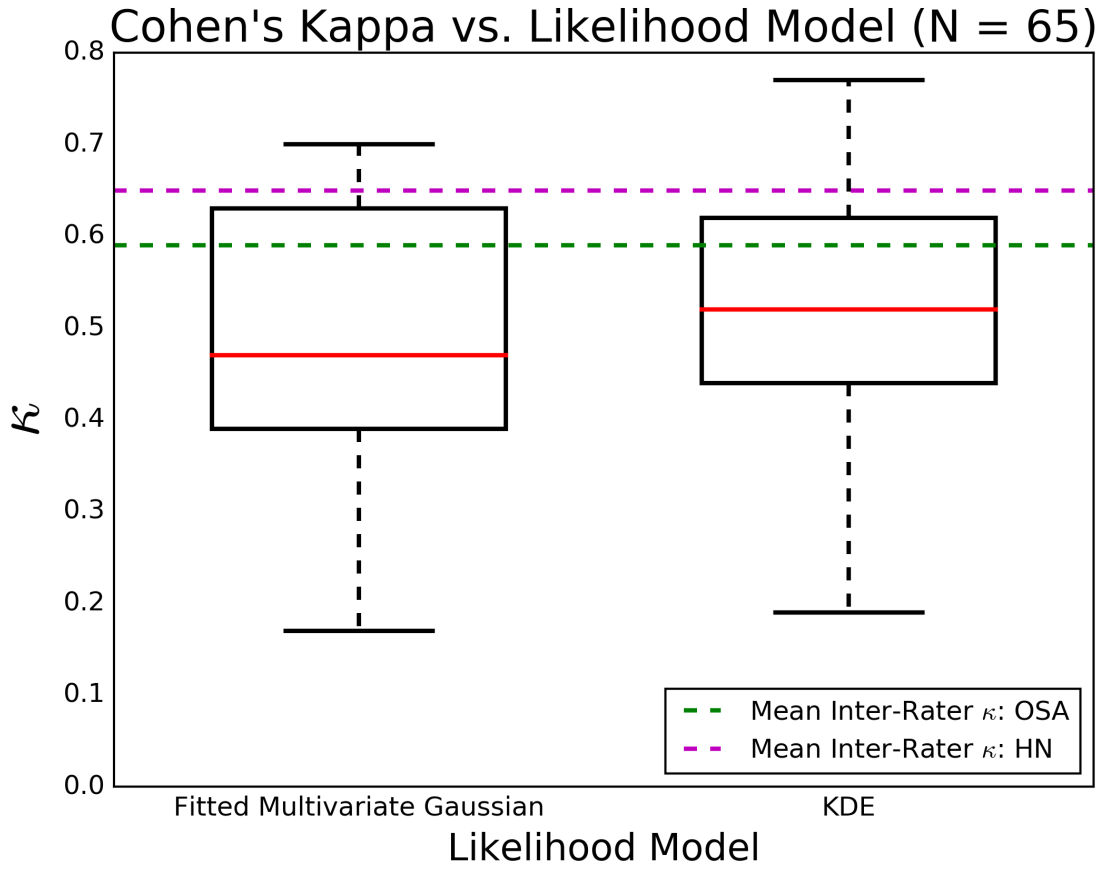

Figure 3.8: Box plots of per-night Cohens Kappa values, for two likelihood models: fitted multivariate Gaussian and density estimation. Red line = Median. Box edges = 1st and 3rd Quartiles. Whiskers = (1.5 x IQR). Dashed green and magenta lines = mean inter-rater Cohens Kappa between two experts using full PSG in HN and OSA subjects, respectively [14].

The framework utilizing density estimation exhibited a slightly higher median ($\kappa = 0.52$) than the alternative using a fitted Gaussian ($\kappa = 0.47$). Median values for both frameworks would classify as fair agreement, and were in the same agreement domain as the mean inter-rater agreement between two experts scoring sleep in OSA ($\kappa = 0.59$). The inter-quartile range (IQR) of the density estimation model was also narrower, suggesting less variability in the models ability to classify accurately whole-night sleep architecture. Moreover, whisker edges of the density estimation-based model were both higher than the fitted Gaussian approach, with the 4th quartile of κ values entirely higher than the mean inter-rater κ for OSA.

When only inspecting the OSA_{UCSD} results, the median κ and IQR for the fitted Gaussian were 0.43 and 0.15, respectively, while for the density estimation approach were 0.48 and 0.15, respectively. These results suggest that density estimation procedures have the potential to better statistically encode the structure of sleep, and thus are appropriate for use in single-channel automated sleep scoring. In addition to per-night assessment of the density estimation-based algorithm, sensitivity and specificity values were calculated on a per-epoch basis. Table 3.2 displays a 5-stage confusion matrix between Clinical and Algorithm scores for each of the 60,903, 30s epochs of sleep. The following is the true per-stage breakdown of the 30s epochs: W_c = 14,582, R_c = 7,105, $N1_c$ = 11,398, $N2_c$ = 23,021, $N3_c$ = 3,797.

Table 3.2: Confusion Matrix for epoch-by-epoch comparison of Clinical PSG-based sleep scoring vs. Algorithm scoring.

		Algorithm					
		W_A	R_A	$N1_A$	$N2_A$	$N3_A$	*Sensitivity*
Clinical	W_C	**12,367**	783	1,132	261	39	85%
	R_C	466	**5,651**	646	308	34	80%
	$N1_C$	2,059	2,556	**4,823**	1,894	66	42%
	$N2_C$	913	2,586	3,913	**12,815**	2,794	56%
	$N3_C$	35	22	12	426	**3,302**	87%
	Specificity	78%	49%	46%	82%	53%	

Using a single-channel of EEG, the proposed algorithm performed exceptionally well in per-epoch recall of stages W, R, and N3 (85%, 80%, and 80%, respectively). Recall that the mean inter-rater agreement for OSA data is just above 70%; by this metric, the sensitivities for W, R, and N3 were on-par with full PSG expert scoring. Stages N1 and N2 reported lower sensitivities values (42% and 56%, respectively). This is expected for stage N1, as it often resembles stages W and R; this misclassification is evident in the spread of W-R-N1 values in the

confusion matrix.

Regarding precision, the algorithm performed best in stages W and N2 (78% and 82%, respectively), with the remaining three stages reporting values between 45-55%. For stage R, the lower specificity is accounted for by misclassifications of stages N1 and N2, while stage N1 was misclassified most as N2 and R. For stage N3, specificity was low due to misclassification with stage N2, though algorithm sensitivity for stage N3 was high.

3.4.5 Algorithm Performance vs. OSA Severity

To determine the effect of OSA on algorithm performance, the per-night κ values generated via the density estimation-based algorithm were compared across healthy/normal (N = 15), mild (N = 9), moderate (N = 9), and severe OSA (N = 32) categories (Figure 3.9). Overall, the downward trend of as a function of OSA severity was modest, which indicates a robustness in the algorithms ability to score appropriately degrees of fragmented sleep architecture.

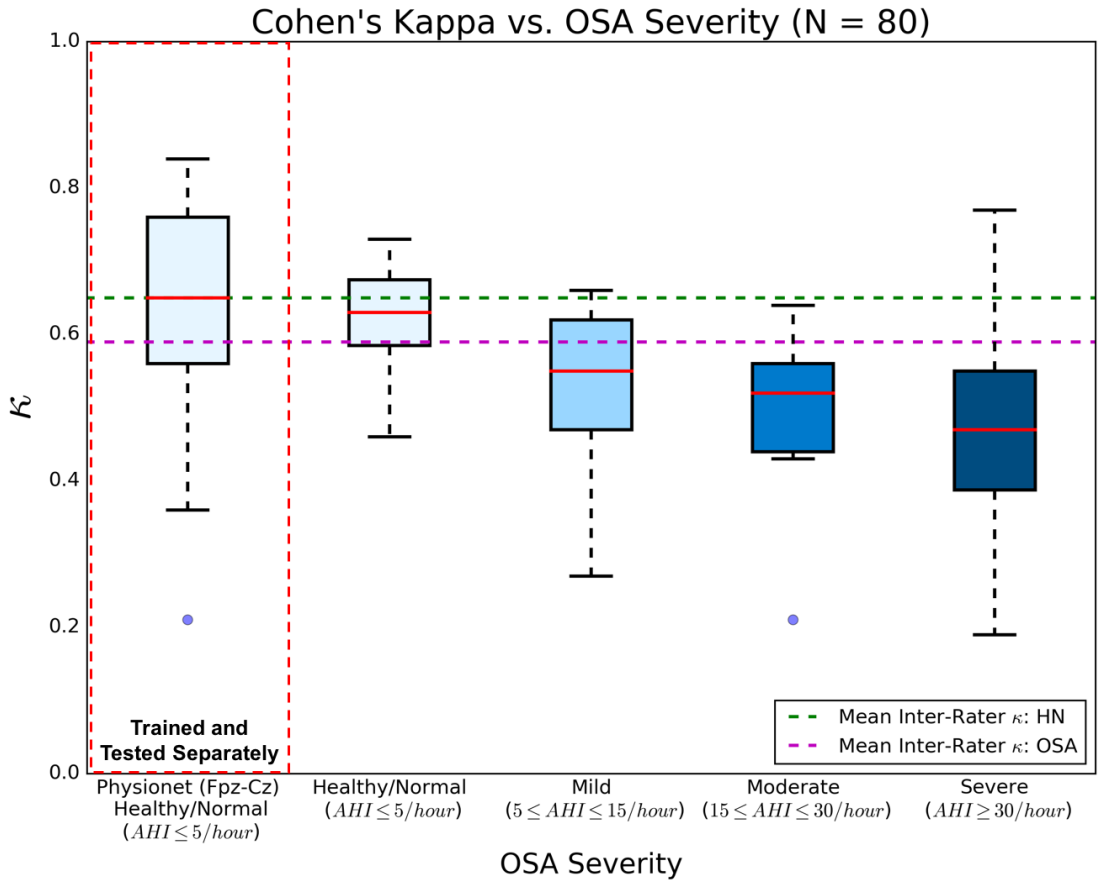

Figure 3.9: Box plots of per-night Cohens Kappa values, for four categories of OSA severity. All values were generated via the density estimation-based algorithm. $HN_{Physionet}$ Fpz-Cz data were trained and tested separately.

Data extracted from Physionet were separately used for algorithm training and whole-night sleep architecture classification, using the five-fold cross validation method described above. The $HN_{Physionet}$ data (N = 15) were trained and tested separately due to the difference in sensing montage (Fpz-Cz) used to acquire the public EEG data. The results of the $HN_{Physionet}$ analysis are also illustrated in Figure 3.9, juxtaposed with HN_{UCSD} results to indicate the algorithm performance based on differing healthy/normal EEG acquisition. Using the Fpz-Cz single-channel data, the algorithm produced a median κ exactly equal to the mean inter-rater agreement between two experts scoring sleep in HN subjects ($\kappa = 0.65$). Alternatively, to test the generalizability of the trained algorithm, $HN_{Physionet}$ data was used as test data in the F3-A2-trained algorithm. As expected, algorithm

performance on the $HN_{Physionet}$ data dropped to a median $\kappa = 0.47$, with an interquartile range (IQR) = 0.31, similar to the results for severe OSA F3-A2 data. Still, more than half of the $HN_{Physionet}$ classification was considered to be in at least fair agreement, which suggests the algorithm is able to reconcile similar sleep EEG features in data from different sensing montages.

In addition to stratifying performance across OSA severity, κ values were further partitioned based on sleep stages, from whole-night sleep architecture results. Figure 3.10 illustrates the stage-specific algorithm performance with increasing OSA severity. Only HN_{UCSD} and OSA_{UCSD} data was included (N = 65). As expected, per-stage performance trends downward as OSA increases from HN to severe OSA. An exception here is stage N1, which exhibits a modest increase in κ spread, the largest occurring for severe OSA classification. Stages W, R, and N2 maintain median κ values in at least fair agreement across OSA severity, with a large increase in IQR for stage R in the severe case. Stage N3 appears as the most variable in performance, with an abrupt drop in median κ upon transition from mild to moderate OSA. Despite this, about one quarter ($\approx$ 8 nights) of all N3 values for severe OSA lie within the fair/high agreement range. This observation, combined with sustained values in the other stages of sleep, further suggests the single-channel algorithm demonstrates classification robustness across OSA severities.

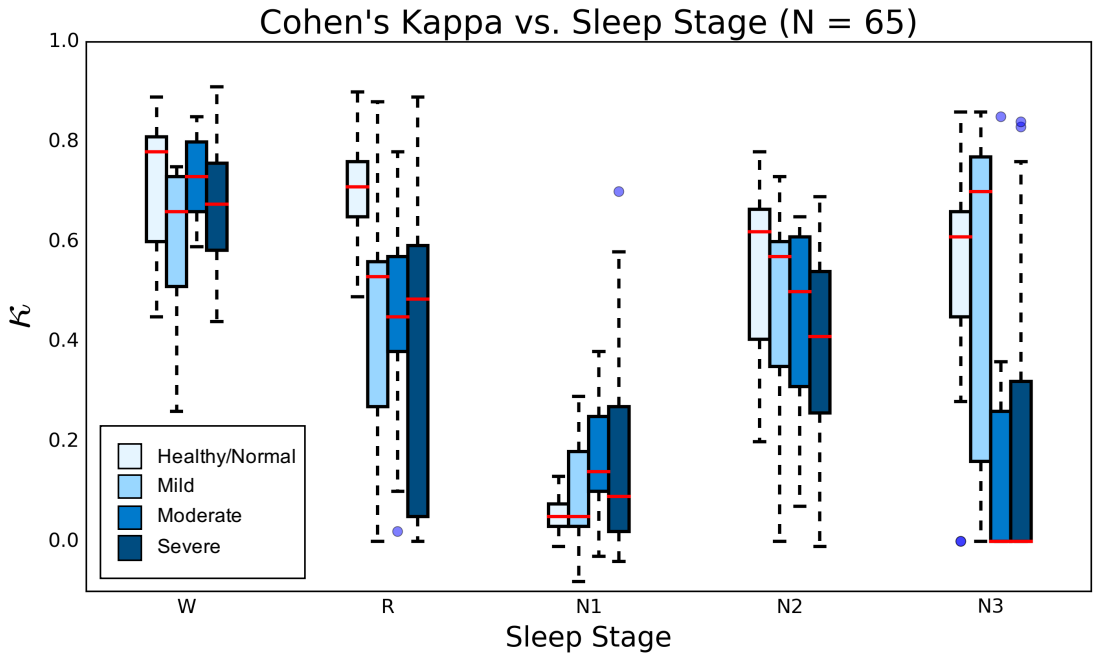

Figure 3.10: Box plots of per-night Cohens Kappa values, for each stage of sleep and across OSA severity. $\text{HN}_{\text{Physionet}}$ data not included.

3.5 Discussion

To improve the current state of automated sleep scoring and provide a means for assessing pathological sleep, an algorithm is presented that utilizes a limited physiologic dataset (i.e. single-channel EEG) to estimate whole-night sleep architecture in OSA and HN subjects. The algorithm makes use of KDE to generate statistical models based on single-channel sleep EEG spectral features, and a HMM to formulate whole-night sleep architecture as a state space, transition-constrained process. Few studies have focused automated sleep scoring efforts on OSA subjects [92,94,106,108], and none have implemented a multimodal statistical framework such as that presented here for investigating OSA sleep architecture. The results of this study indicate that this statistical approach to scoring sleep in OSA subjects with single-channel sleep EEG is effective and promising as a means to emulate expert-level scoring in an automated fashion.

Spectral EEG features were generated via the MT spectrogram, which has

been shown to produce more accurate spectral estimates of EEG, as compared to the standard FFT, wavelet transform, and other spectral decomposition techniques [112, 114]. Each feature was extracted to embody the rules used for visual scoring of sleep EEG, specifically extracting the activity in EEG frequency bands that possess information about each or a combination of the five stages of sleep. For example, a 0.1-50Hz *broad* power feature was used to quantify motion artifact as sharp deflections spanning most frequency bands in the recorded EEG, which typically appear during stage W and at the onset of arousal. Other well-known EEG rhythms (e.g. α, θ, and δ) were used to quantify activity in corresponding characteristic sleep stages, as per Table 3.1. Unique to this work is the separation of the α band into four 1Hz bands (α_1-α_4) to capture the nuanced α activity in stage R, which is expected as a 1-2Hz slower α rhythm compared to stage W [88].

To develop the distribution of spectral features within each stage of sleep, density estimation was used over standard fitted Gaussian approaches. Specifically, KDE was implemented to generate likelihood estimates capturing multimodal structure of the joint density surface in regards to spectral variability within a stage of sleep. For example, approximately 20% of the adult U.S. population generates little or no α activity during wakefulness [88, 127]. In this context, a standard Gaussian model might not accurately represent both the presence and absence of α activity within stage W, incorrectly approximating a bimodal distribution as a single over- smoothed mode in the domain of α activity. In addition, multi- modal statistical modeling of sleep stages can begin to quantify the errors/variability in human sleep scoring within sleep stages. Since visual, per-epoch sleep scoring is not an exact science, small variations in intra-stage human sleep scoring can manifest as large discrepancies in standard Gaussian modeling, resulting in poor algorithmic sleep scoring performance.

Figure 3.4 and Figure 3.5 illustrate univariate histograms of all eleven spectral features (Table 3.1) for each sleep stage, depicting the unimodality of HN sleep EEG and the sometimes subtle changes in EEG spectra as OSA subjects go into deeper modes of sleep. In some instances, a standard Gaussian would represent the data distribution accurately (e.g. most HN sleep and the unimodal distribu-

tions of β and vlf features in most stages for OSA). Conversely, other features – in particular, γ, δ, σ, and θ – exhibited distinct multimodal structure across all stages of OSA sleep, which cannot be correctly captured by the standard Gaussian (Figure 3.6).

In OSA, each of the four α band features extracted display a transformation from unimodal, skewed Gaussian-like structure in stage W, to bimodal structure in the positive PSD domain during stage N3. This is interesting since α-type rhythms are not typically considered key indicators of deeper sleep, yet distinct peaks centered around 0dB and 30dB are present in N2 and N3 sleep, the latter value of which is similar to that in stage W and stage R. This suggests that the histograms (and as a consequence, the KDE likelihoods) capture two different populations of spectral EEG – one centered about 0dB and another centered about 30dB. The former might portray the typical suppressed EEG signature of α activity in N2-N3 sleep, while the latter might reflect an increase in activity related to respiratory-based arousals and increased sympathetic activation during these epochs of sleep in OSA subjects [8].

Sleep architecture was modeled as a HMM transition-constrained process, with conditional likelihoods dictating physiologic transitions during sleep. Previous work in the literature has used HMM to model and score sleep [98–103], though none has focused on multimodal class conditional densities, nor have they exclusively focused on OSA subject data as used in the proposed HMM framework. The 5-stage transition values used in the HMM were extrapolated from previous work on a 4-stage transition model – Wake, REM, Light (N1/N2), Deep (N3) – of sleep in OSA subjects [124]. Specifically, the presented algorithm implemented transition likelihoods for N1 and N2, each stage with identical transition probabilities to ensure parity when expanding the light stage values to the new 5-stage model. Transitions between N1 and N2 were made more probable (e.g. $Q_{i,j} = 0.20$), compared to transitions to other stages (e.g. $Q_{i,j} = 0.10$), to reflect the increased fragmentation and wake-sleep characteristics of sleep in OSA subjects.

Cohens kappa values for per-night, KDE-based classification of sleep architecture are shown in Figure 3.8. Values range from $\kappa = 0.20$ to $\kappa = 0.77$, with

a median $\kappa = 0.52$ and more than three quartiles of the values demonstrating at least fair agreement in classification accuracy when compared to expert-scored hypnograms. For perspective, the mean inter-rater Cohens kappa between experts scoring with full PSG in HN and OSA patients is $\kappa = 0.65$ and $\kappa = 0.59$, respectively [14]. [6]. While the fitted Gaussian model also produced κ values in fair agreement, this is suspected to be due largely in part to the inclusion of HN EEG datasets, which stand to benefit less from a density estimation-based approach when a simpler unimodal Gaussian will suffice, as depicted in Figure 3.5. It seems that density estimation plays a smaller role in improving sleep scoring in HN subjects, instead excelling when implemented on sleep that is heavily fragmented (such as in OSA). These results suggest that the proposed algorithm performs quite well in scoring sleep architecture in a mix of HN and OSA sleep, despite only using a single channel of EEG data.

Further investigation of algorithm performance revealed a modest inverse relationship between per-night κ agreement and OSA severity (Figure 3.9). Increased sleep fragmentation equates to more wake-sleep transitioning and a general difficulty in sleep architecture classification. While agreement between the algorithm and clinical scoring decreases as OSA severity increases, Figure 3.9 illustrates that the algorithm achieved fair agreement values above $\kappa = 0.50$ for almost half of the 32 total nights of sleep with severe OSA. An example of the algorithms ability to accurately classify sleep architecture in a subject with severe OSA (AHI = 63.1 events/hr) is shown in Figure 3.7. Further speaking to performance on HN data, results from a separate 5-fold cross validation on $\text{HN}_{\text{Physionet}}$ data (Figure 3.9) show that the algorithm works equally well on data derived from another EEG montage (i.e. Fpz-Cz), emphasizing the generalizability of the described methods. This suggests that the algorithm may not only be robust to certain degrees of OSA severity, but can also be improved to appropriately score sleep in a manner agnostic to sleep fragmentation and EEG acquisition.

A stage-specific analysis of the combined HN_{UCSD} and OSA_{UCSD} results further revealed modest deterioration of the algorithmic single-channel scoring for increasing OSA severity (Figure 3.10). As expected, results for stages W, R, and

N2 are primarily in good agreement, with little deterioration across OSA severity. Interestingly, stage N1 agreement increased slightly as AHI increased, running counter to other sleep stages. As OSA worsens, an increase in sleep fragmentation generally leads to an increased frequency of stage N1, as patients arouse from sleep more often throughout the night. As a consequence, EEG spectral features related to stage N1 may become more prominent, which may accommodate increased classification accuracy of stage N1 in this analysis.

An increase in N1 scoring during OSA would elicit an infrequency of other sleep stages for the same total sleep time, such as stage N3 and stage R (whose specific discrimination from N1 is already difficult in HN patients). For stage N3, many agreement values in moderate and severe OSA dropped dramatically to $\kappa = 0.00$, though some values extend past fair agreement and well into high agreement. The same occurs in stage R for mild and severe OSA. Based on the large degree of κ spread, it appears low Cohens κ values not only arise from sheer misclassification between two classes, but also from an uneven distribution of samples between two classes (e.g. in a whole night of sleep, $R_c = 25$ epochs, Non-$R_c = 600$ epochs). The result is a trade-off in stage-specific κ performance due to OSA severity, specifically with infrequent sleep stages demonstrating a high agreement due to chance, which by virtue of the numerator of equation 3.6, results in a low κ score. This happens to be an example of low κ values resulting from imbalance/low prevalence of an observation, a limitation of Cohens κ which has been discussed extensively in the literature [128].

Whole-night classification results demonstrate improved N1 scoring over the literature, while maintaining high degrees of classification for other sleep stages. This suggests that the algorithm has the potential to accurately and automatically generate desirable sleep metrics such as Total Sleep Time, Wake After Sleep Onset, and Sleep Efficiency. Even so, improvement is necessary, in particular to address the difficulty in classification for datasets with increased N1-N2 transitioning. As discussed, this is a general problem of automated sleep scoring, even for scoring in HN subjects, demonstrated by low-sensitivity results for N1 staging in the single-channel algorithm literature [91, 92, 95, 98, 105, 106, 108, 109].

Another area to be addressed is the algorithm sensitivity and specificity between stages N2 and N3. Differences in the accuracy of N2-N3 scoring have been observed before, in particular the over-scoring of N3 compared to N2 for data derived from frontal sensors, as compared to central derivations [129]. More generally, a marked difference in N2-N3 scoring has been observed between automated and manual scoring of sleep [93]. It is difficult to ascertain if automated algorithms such as the proposed are incorrectly scoring N2-N3 epochs of sleep, if the discrepancy is due solely to bias in the manual scoring performed by the expert, or a combination of the two. Because an automated algorithm can quantify minute differences in EEG (e.g. presence and strength of delta waves) more easily and efficiently than a visual scorer, it has been suggested that automated scoring is possibly more precise in N2-N3 classification [93].

The presented work utilized the MT spectral estimate to generate and extract frontal EEG spectral features. Implementation of novel spectrotemporal decomposition techniques [67] might serve to improve algorithm performance through integrated knowledge of the sparse macrostructure of sleep EEG when rendering spectral estimates. Regarding EEG- based features, frontal EEG-derived eye movement and K-complex information can be extracted via cross-correlation approaches to improve the specificity in scoring stages R and N2, respectively [130,131]. Moreover, a natural extension of the proposed work is the automated detection of arousals and apneas/hypopneas based on single-channel/limited physiologic data streams. A method for detection of relevant sleep phenomena, and subsequent generation of clinical criterion for OSA screening, could be formulated by closer inspection and characterization of the multimodal distributions of EEG spectra described here. By using appropriate statistical methods that accommodate multimodal distributions, it may be possible to categorize an arbitrary epoch of sleep EEG as HN or OSA-like. Moreover, it may be possible to use such per-epoch categorizations to estimate whole-night OSA severity. As such, the resulting paradigm, using only single-channel EEG, has the potential to serve as a surrogate for clinical assessment of arousal indices or AHI. In addition, it may even help characterize different phenotypes of OSA and other sleep disorders.

Finally, to facilitate frontal-based sensing of physiologic signals during sleep, novel technologies in the field of wearable sensors and systems [15, 23, 132] can be leveraged as tools for unobtrusive, peel-and-stick sleep monitoring. Combined with low-resource algorithms – such as the proposed statistical methods – wearable systems can begin to monitor sleep objectively, thus allowing clinical metrics that go beyond the current standard of subjective recall.

3.6 Conclusion

New technologies have the potential to disrupt the clinic, and the field of Sleep Medicine may be able to move beyond the limitations of the gold standard PSG through smaller and more efficient devices for recording and generating clinical sleep metrics. While the recent surge of minimalistic, at-home sleep monitoring devices aims to improve Sleep Medicine practices, these endeavors lack analytic techniques that efficiently estimate sleep architecture from reduced data streams. This work outlines a statistical framework for classifying whole-night sleep architecture from single-channel EEG spectral features. The algorithm formulated sleep architecture and the five clinical stages of sleep as a transition-constrained, state space process with intra-stage multimodality in the domain of EEG spectra. Results of the study show the algorithm is able to utilize single-channel EEG to automatically discriminate and score whole-night sleep architecture in both HN and OSA sleep, in many cases with high Cohens kappa agreement, when compared to clinical scoring from experts using full PSG. Moreover, the algorithmic approach sustains fair scoring agreement for increased OSA severity, demonstrating potential for generalizability and objectivity in the evaluation of the many intricacies of sleep and sleep disorders. This is one of just a few studies that have implemented state space modeling for single-channel sleep scoring, and the first known study to implement such statistical methods for automated sleep architecture performance in OSA subjects. The continued development of such low-resource algorithms – guided by clinical expertise and emphasizing clinical practicality – will help realize automated tools for assessing sleep and sleep disorders in inpatient and outpatient

populations.

3.7 Acknowledgements

Chapter 3, in full, is a reprint of the material as it appears in *IEEE Transactions on Biomedical Engineering* 2017. Kang, Dae Y.; DeYoung, Pamela N.; Malhotra, Atul; Owens, Robert L.; Coleman, Todd P., IEEE, 2017. The dissertation author was the primary investigator and author of this paper.

This research was supported by the National Heart, Lung, and Blood Institute (3R01HL085188-07S1), and the National Institute of General Medical Sciences (R25GM083275-09).

Chapter 4

Objective and Automated Assessment of Clinical Sleep and Sleep Disorders

Chapter 4 presents on-going work that seeks to specialize the sensors work in Chapter 2, for specific applications in robust measurements of low-frequency electrophysiology (e.g. EEG) in long-term sleep monitoring. In addition, Chapter 4 discusses an analytical strategy inspired by the methodology in Chapter 3, for attaining a surrogate measure of the apnea-hypopnea index, the primary metric for determining presence and extent of OSA.

4.1 Towards A Peel-and-Stick Monitoring System for Continuous Sleep Electrophysiology

To advance the engineering findings from Chapter 2, much work has been performed on the advancement of stretchable electronics for use in unobtrusive, objective sleep and OSA monitoring. Specifically, efforts in regards to stretchable sensor development and a rigid-to-stretch physiological monitoring system have been pursued simultaneously.

As discussed in Chapter 2, Au stretchable sensors can be integrated seam-

lessly into peel-and-stick adhesives and used as sensors for measuring biosignals such as EEG. To further demonstrate their utility, these sensors are currently being implemented for whole-night sleep EEG acquisition. Figure 4.1 illustrates a (un-wired) two-channel EEG sensing montage adhered to the forehead of a patient to undergo a full PSG study. The Au sensors were positioned with channels 1 and 2 at the Fp1 and Fp2 positions, and reference and ground sensors positioned along the midline of the forehead.

Stretchable sensor positioning was intentional, to confine the current and future monitoring schemes to the forehead. The forehead is an attractive real estate for biopotential sensing, as it is mostly devoid of hair, and typically does not experience heavy motion artifact during sleep, such as tossing and turning on a pillow. Additionally, it is possible to use reflectance pulse oximetry to record oxygen saturation (SpO_2), a typical biosignal used in full PSG and a signal vital in the assessment of apneas and hypopneas [8]. Lastly, as the forehead is openly exposed to the environment, measurement of environmental cues/factors, such as exposure to light, can be gathered on the same real estate during sleep monitoring.

A 15-second snapshot of raw sleep EEG recorded using one of the two Au stretchable sensor channels is also shown (green time series), aligned with corresponding EEG from a conventional gel sensor (red time series). Here, the Au stretchable sensor was able to capture the signature EEG characteristics of certain sleep stages, namely the K-complex and sleep spindle combination specific to stage N2, as well as the rapid eye movement deflection specific to the similarly named stage REM.

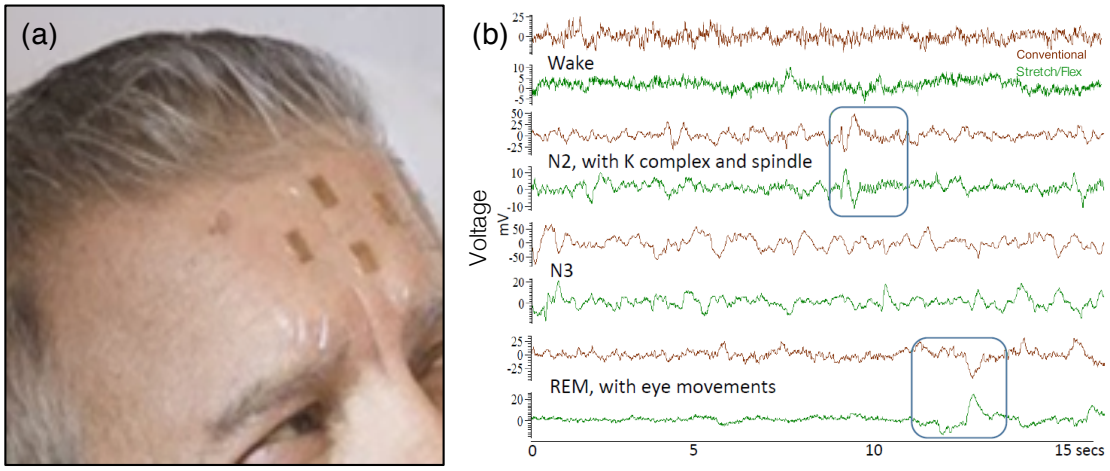

Figure 4.1: **a)** Two-channel, stretchable EEG sensor system applied via peel-and-stick clinical adhesive for seamless, all-frontal sleep sensing. **b)** Raw EEG data from a clinical overnight polysomnogram using wired conventional sensors vs. wired adhesive-integrated stretchable sensors.

While capable of acquiring biopotential activity in the form of EEG and other biosignals, Au-based stretchable films are not perfectly suited for sensing electrophysiology, due to issues of steady drift and charge accumulation at the sensor-skin interface [65]. These issues of drift are most pervasive at lower frequencies, in the domain of EEG rhythms ($\leq$ 100Hz). Moreover, because noise due to drift potentials worsens as a function of time, measurements during whole-night sleep recordings are susceptible to this effect. Figure 4.2 illustrates a multitaper spectral estimation of EEG recorded via Au stretchable sensors during a short period of sleep (approximately 3.5-hours), during which steady drift is apparent in the δ band.

To advance the utility and robustness of stretchable sensors for low-frequency electrophysiological monitoring, the microfabrication methods discussed in Chapter 2 have been implemented to create stretchable Ag/AgCl stretchable sensors (Figure 4.2). As mentioned previously, Ag/AgCl sensors are the standard electrode used in electrophysiology, due to their superior electrode stability and DC coupling [65]. For this reason, and because Ag (like Au) is a noble metal with generally poor adhesive properties, there was motivation to microfabricate Ag/AgCl stretchable sensors using the methods described in Chapter 2. Specifically, the

Ag/AgCl methodology was almost identical to what is illustrated in Figure 2.2, only that the metallization of Au onto the weak-adhering elastomer was replaced with pure Ag. An additional post-processing step is added after the peel-off step — $FeCl_3$ is used to chemically chlorinate the pure Ag surface, thus forming a thin layer of AgCl [133]. The result is a new stretchable sensor for which the same processes can be used in microfabrication and integration into clinical adhesives.

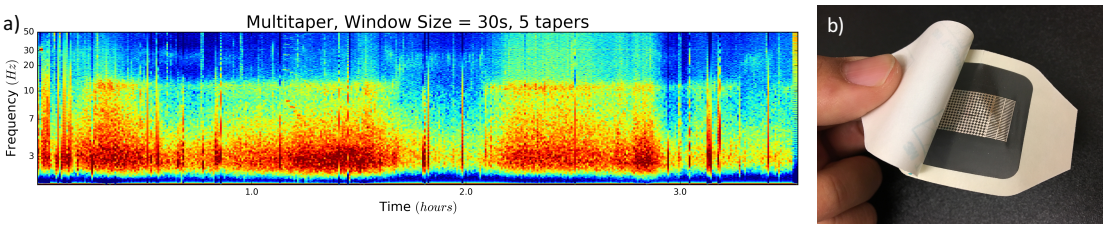

Figure 4.2: **a)** Snapshot of sleep EEG measured using wired Au stretchable sensors. Note the steady drift in the δ band. **b)** Stretchable Ag/AgCl sensors for robust low-frequency electrophysiological monitoring, mounted integrated into 3M Tegaderm^{TM}.

To this end, current work includes characterization of the new sensor properties (e.g. impedance spectroscopy) and the change in mechanical interaction between the substituted Ag metal and the carrier elastomer (peel and adhesion tests). After fine-tuning, the stretchable Ag/AgCl sensors will be implemented in in-lab sleep studies, to measure sleep EEG against conventional Ag/AgCl sensors typically used in full PSG. The sensors will be feed sleep EEG into a rigid, credit card-sized wearable bioinstrumentation amplifier capable of 10-12 hours of continuous 8-channel recording, local microSD card storage, and Bluetooth transmission. This system was designed with components that have smaller packaging, and is envisioned to be scaled into a solderable, stretchable circuit board on clinical adhesive, as demonstrated in Kim et al. 2017 [134]. Finally, additional tests will be performed to investigate the utility of these sensors for robust measures of gastric slow wave activity, which stands to benefit from stretchable Ag/Agcl sensors as the biosignal manifests at a much lower frequency than EEG [135].

4.2 Automated OSA and arousal detection via single-channel EEG

Alongside stretchable sensor and electronics design for unobtrusive sleep monitoring, the findings discussed in Chapter 3 are currently being re-implemented for automated analytics in OSA. As shown before, Figure 3.4 in Chapter 3 illustrated the histogram distribution of extracted EEG feature power spectral densities, stratified by sleep state for a combination of healthy/normal (HN) subjects and OSA patients. Similarly, Figure 3.5 illustrated the same type of data, this time only for HN subjects. The apparent difference between both figures is the location of the histogram peak(s) along the PSD axis — in NREM stages of sleep and lower-frequency rhythms (e.g. θ and δ), the mode of distribution seems to shift to the left in OSA patients, as compared to the HN group. Conversely, the higher-frequency rhythms (e.g. γ and β) shift to the right in OSA patients, as compared to the HN group.

To venture an educated guess about this observation: as sleep in OSA is typically fragmented and lacking of undisturbed sleep, the characteristic changes in EEG rhythms expected of increasing depth of sleep are lost. The result might look like a downward shift in low frequency spectral features observed, to appear as "weak" and unstable stages of sleep, akin to what is pictured in Figures 3.4 and 3.5. Should this be the case, it might be possible to discern the epochs of sleep data belonging to the class of HN-type sleep and those that more closely resemble OSA-type sleep — a binary classification possibly indicating OSA presence and severity. Potentially, this method can render a surrogate measure of the apnea-hypopnea index (AHI) and/or the respiratory disturbance index (RDI), using only a single channel of sleep EEG.

To investigate this, the distribution of EEG spectral features were marginalized along the sleep stage axis, since most features in Figure 3.4 maintain bimodality across all sleep stages. Figure 4.3 illustrates the marginalized distributions for each single-channel EEG spectral feature from Figure 3.4. With exception of the β and *vlf* features, all other features exhibit distinct peaks along the PSD axis.

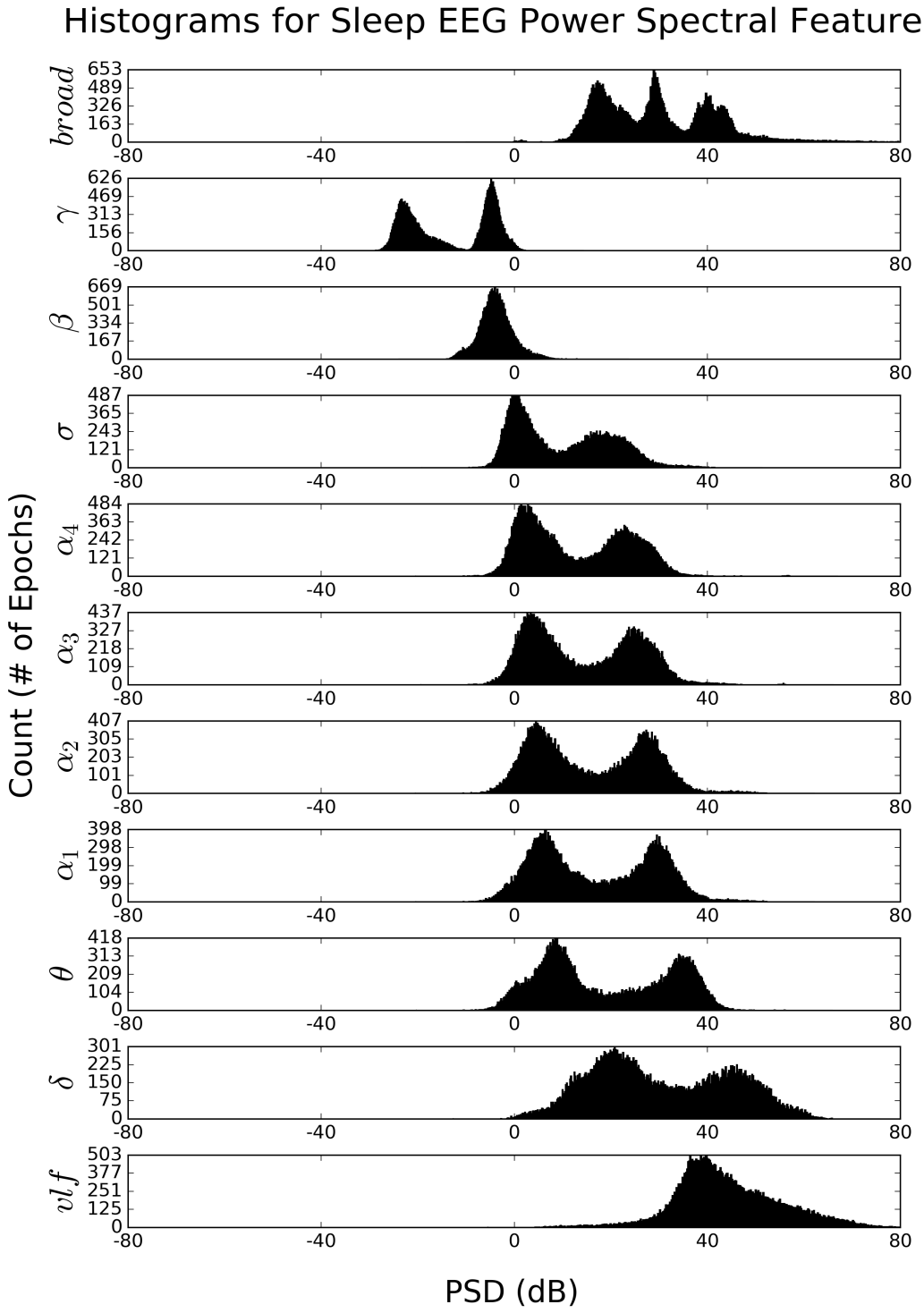

Figure 4.3: Histogram of single-channel EEG spectral features in HN and OSA subjects, marginalized across sleep stages. Distinct modes appear for most EEG spectral features, suggesting there is a contributing factor to EEG variability beyond sleep stage.

Figure 4.4 illustrates the marginalized distribution for the γ EEG feature. In this plot, there is a clear position along the PSD axis at which a hypothetical line can be drawn. Perhaps, for the higher frequency γ rhythm, anything to the left of the boundary (i.e. decreasing in PSD) belongs to the class of HN-type sleep, while any epoch of EEG data that falls on the right is categorized as OSA-type sleep. While one expects the γ rhythm to decrease during HN NREM sleep, the epochs of increased activity seen here may be contributed by cortical arousals related to respiratory disturbances and a general disposition of wakefulness, which is characteristic of OSA.

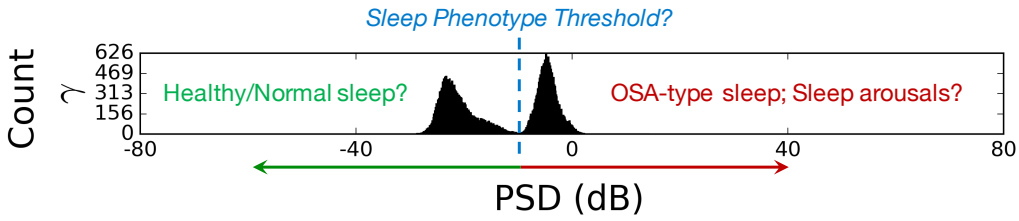

Figure 4.4: A possibility for sleep epoch phenotyping via thresholding of frontal EEG power spectral density. Single-channel sleep EEG revealed bimodal structure in the γ spectrum, which may indicate discriminatory sleep signatures specific to OSA and/or respiratory-induced sleep arousals.

Though the data requires more teasing, the simple histogram/density estimation approach utilized in Chapter 3 could provide great insight here beyond its use in automated sleep staging. Clearly, the data is telling a story in sleep EEG variability, possibly due to other confounding variables such as age and sex. Pending that this bimodality remains in the EEG distributions after accounting for all other covariates, a next natural step is to crudely classify sleep EEG epochs as HN or OSA through a decision boundary as in Figure 4.4. Then, after performing this classification for all epochs in a whole night of sleep, take the sum total in each category and correlate these values to the subject's AHI and RDI values for the same night.

More appropriately, the same data will be used in a testing-training paradigm involving logistic regression, with the rails of the logistic function representing HN and OSA-type sleep. In this manner, it is possible to receive a probability asso-

ciated with the HN/OSA categorization of an arbitrary epoch of sleep, which can be further implemented as the likelihood model in a simple 2-state HMM, akin to what was discussed in Chapter 3. To this end, and if the biomodality appears to be caused by OSA phenomena such respiratory-based arousals, then it is astute to consider the time dynamics and frequency of arousals during a night of sleep in OSA. Specifically, a state space transition model for sleep arousals will be generated, such as that depicted in Figure 3.2. Figure 4.5 portrays the Arousal-No Arousal transition dynamics in a single night of sleep for an OSA patient. Here, each epoch of sleep was scaled down to 2s. This is appropriate as sleep arousals (unlike sleep stages) are not clinically labeled on a 30s basis — each labeled arousal lasts at least 3s, upwards to 15s in length, after which point the epoch of sleep during which this arousal occurs becomes stage Wake. By deconstructing clinically-scored sleep in this manner, an algorithm will not only be trained to identify sleep arousals from single channel EEG, but will also constrain the dynamics of sleep arousal transitions to what is expected in the sleep physiology of OSA — for example, the propensity to remain in a sleep aroused state during an unaided apneaic/hypopneaic episode. This, in combination with automated sleep staging from the same EEG signal, could supplant the need for multi-channel, multi-sensor data to provide seamless measures of sleep and sleep breathing disorders.

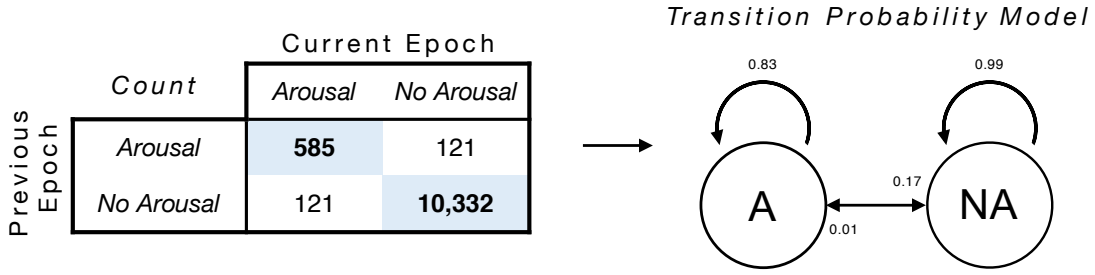

Figure 4.5: Example of an empirical transition model of sleep arousals occurring in consecutive 2s epochs during a single night of sleep.

4.3 Acknowledgements

Chapter 4, in part is currently being prepared for submission for publication of the material. Kang, Dae Y.; Malhotra, Atul; Owens, Robert L.; Coleman, Todd P. The dissertation author was the primary investigator and author of this material.

This research was supported by the National Heart, Lung, and Blood Institute (3R01HL085188-07S1), and the NSF-supported San Diego Nanotechnology Infrastructure (SDNI) of UCSD (ECCS-1542148).

Chapter 5

Conclusion

Although the importance of sleep is increasingly recognized, especially as short sleep duration becomes more commonplace, the dearth of robust, non-invasive systems for objective sleep measurement hinders our understanding of the sleep process, and its role in health and disease. Current methods for measuring sleep are fraught with expensive equipment and cumbersome sensing montages that interfere with sleep. To make matters worse, interpretation of recorded signals involves mundane and specialized visual/manual analysis, often resulting in subjective results and modest variability between sleep experts. With nearly 40% of US adults experiencing problems with sleep, and many millions of individuals invisibly suffering from OSA, the broad measurement and understanding of sleep is quickly becoming a necessity for appropriately addressing these public health issues.

The rise of new wearable health devices promises broad usability and a means for collecting troves of ambulatory health data. Such are poised to replace the PSG and other bulky and subjective tools for physiological monitoring. Though today's devices trend towards new and miniaturized platforms for sleep monitoring and other related applications, their utility has only been demonstrated in the consumer markets, for which stringent clinical testing and approval are lax, at best. Moreover, in regards to sleep, developments in software and analytics lag behind the hardware innovations, such that devices do not provide measures of sleep that are on-par with clinical PSG scoring. That is not to say that wearable devices cannot achieve this level of clinical exactness, but that there is a lack of

analytical tools capable of interpreting these reduced data streams. To put it plainly, one cannot get something from nothing. To address these shortcomings in Sleep Medicine, and to aid in the advances of wearable electronics, this dissertation sought to develop a suite of tools towards the non-invasive sensing and objective analysis of sleep and sleep disorders.

First, a thought on clinical usability and an unlikely fabrication method enabled the engineering and integration of stretchable sensors into peel-and-stick clinical adhesives. The results of this work were robust sensors through which quantities such as EEG and mechanical strain could be sensed, and for which said sensors could be created in a scalable manner while improving sensor quality. Current work looks to generalize these methods for the microfabrication of other stretchable sensors, made of metallic materials that are more suitable for the application of whole-night sleep monitoring. Of interest are stretchable adhesive sensors for the acquisition of low-frequency electrophysiology, which encompasses sleep EEG rhythms and includes a relatively unknown (but significant) gastric slow wave.

Second, a shift in the dissertation to machine learning and a collaboration with clinicians in Sleep Medicine lead to statistical analytics for automated assessment of sleep architecture from single-channel electrophysiology. Through the use of non-parametric density estimation, a conditional likelihood model of sleep was generated to faithfully model the ground truth multimodal characteristics of sleep EEG. The use of these likelihoods, combined with a state space dynamical model of sleep, enabled the automated scoring of whole-night sleep architecture. Results using the same model in both healthy/normal and OSA populations yielded at least fair agreement with gold standard full PSG scoring, indicating the algorithmic framework is somewhat agnostic to healthy or diseased sleep. The methods used to capture the nuanced structure of sleep EEG is currently being implemented for further automated assessment of respiratory-based arousals and OSA-type sleep. This is to provide objective assessments of sleep disordered breathing from the same single-channel EEG source.

The result of this applied clinical engineering research provides a novel

framework for promoting objective, non-invasive assessments of sleep. Succeeding in just one of the current works will help to improve the materials and methods used in the current clinical sleep paradigm. Accomplishing both could greatly advance the state of the art, by improving objectivity of sleep measurements, improving patient accessibility to clinical-grade at-home sleep testing, and enabling further research investigation into the underpinnings of sleep and its role in health. Ultimately, the dissertation work was formulated and executed to entertain broad applicability of stretchable sensors and analytics for use in all of clinical medicine. The hope is that this co-development of sensors and analytics, guided and motivated by clinicians, would exemplify clinically-guided engineering and serve to advance budding wearable health technologies.

References

[1] Y. Shi and F. B. Hu, "The global implications of diabetes and cancer," *The Lancet*, vol. 383, no. 9933, pp. 1947–1948, 2014.

[2] Precision Medicine Initiative (PMI) Working Group, "The precision medicine initiative cohort program building a research foundation for 21st century medicine," tech. rep., 2015.

[3] B. M. Altevogt and H. R. Colten, "Sleep disorders and sleep deprivation: an unmet public health problem," tech. rep., National Academies Press, 2006.

[4] T. M. Shockey and A. G. Wheaton, "Short Sleep Duration by Occupation Group 29 States, 20132014," *MMWR. Morbidity and Mortality Weekly Report*, vol. 66, pp. 207–213, 3 2017.

[5] M.-P. St-Onge, M. A. Grandner, D. Brown, M. B. Conroy, G. Jean-Louis, M. Coons, and D. L. Bhatt, "Sleep Duration and Quality: Impact on Lifestyle Behaviors and Cardiometabolic Health: A Scientific Statement From the American Heart Association," *Circulation*, vol. 134, no. 18, pp. e367–e386, 2016.

[6] R. Heinzer, S. Vat, P. Marques-Vidal, H. Marti-Soler, D. Andries, N. Tobback, V. Mooser, M. Preisig, A. Malhotra, G. Waeber, P. Vollenweider, M. Tafti, and J. Haba-Rubio, "Prevalence of sleep-disordered breathing in the general population: the HypnoLaus study," *The Lancet Respiratory Medicine*, vol. 3, pp. 310–318, 4 2015.

[7] F. J. Nieto, P. E. Peppard, T. Young, L. Finn, K. M. Hla, and R. Farré, "Sleep-disordered breathing and cancer mortality: Results from the Wisconsin Sleep Cohort Study," *American Journal of Respiratory and Critical Care Medicine*, vol. 186, no. 2, pp. 190–194, 2012.

[8] A. Roebuck, V. Monasterio, E. Gederi, M. Osipov, J. Behar, A. Malhotra, T. Penzel, and G. D. Clifford, "A review of signals used in sleep analysis," *Physiological Measurement*, vol. 35, no. 1, pp. R1–R57, 2014.

[9] A. Rechtschaffen and A. Kales, "A Manual Of Standardized Terminology, Techniques and Scoring Systems for Sleep Stages of Human Subjects," 1968.

[10] C. Iber, S. Ancoli-Israel, A. Chesson, and S. F. Quan, *The AASM manual for the scoring of sleep and associated events: rules, terminology and technical specifications*, vol. 1. American Academy of Sleep Medicine Westchester, IL, 2007.

[11] D. Shrivastava, S. Jung, M. Saadat, R. Sirohi, and K. Crewson, "How to interpret the results of a sleep study.," *Journal of community hospital internal medicine perspectives*, vol. 4, no. 5, p. 24983, 2014.

[12] M. H. Kryger, T. T. Roth, and W. C. Dement, *Principles and Practice of Sleep Medicine (Fifth Edition)*. Philadelphia: Saunders/Elsevier, 5 ed., 2011.

[13] K. J. Finkel, A. C. Searleman, H. Tymkew, C. Y. Tanaka, L. Saager, E. Safer-Zadeh, M. Bottros, J. A. Selvidge, E. Jacobsohn, D. Pulley, S. Duntley, C. Becker, and M. S. Avidan, "Prevalence of undiagnosed obstructive sleep apnea among adult surgical patients in an academic medical center," *Sleep Medicine*, vol. 10, no. 7, pp. 753–758, 2009.

[14] R. G. Norman, I. Pal, C. Stewart, J. A. Walsleben, and D. M. Rapoport, "Interobserver agreement among sleep scorers from different centers in a large dataset.," *Sleep*, vol. 23, no. 7, pp. 901–8, 2000.

[15] D. Y. Kang, Y. S. Kim, G. Ornelas, M. Sinha, K. Naidu, and T. P. Coleman, "Scalable microfabrication procedures for adhesive-integrated flexible and stretchable electronic sensors," *Sensors*, vol. 15, no. 9, pp. 23459–23476, 2015.

[16] R. R. Søndergaard, M. Hösel, and F. C. Krebs, "Roll-to-Roll fabrication of large area functional organic materials," *Journal of Polymer Science Part B: Polymer Physics*, vol. 51, pp. 16–34, 1 2013.

[17] J. P. Metters, R. O. Kadara, and C. E. Banks, "New directions in screen printed electroanalytical sensors: an overview of recent developments.," *The Analyst*, vol. 136, no. 6, pp. 1067–1076, 2011.

[18] S. Harada, W. Honda, T. Arie, S. Akita, and K. Takei, "Fully printed, highly sensitive multifunctional artificial electronic whisker arrays integrated with strain and temperature sensors," *ACS Nano*, vol. 8, no. 4, pp. 3921–3927, 2014.

[19] J. R. Windmiller, A. J. Bandodkar, G. Valdés-Ramírez, S. Parkhomovsky, A. G. Martinez, and J. Wang, "Electrochemical sensing based on printable temporary transfer tattoos," *Chemical Communications*, vol. 48, pp. 6794–6796, 7 2012.

[20] A. J. Bandodkar, D. Molinnus, O. Mirza, T. Guinovart, J. R. Windmiller, G. Valdés-Ramírez, F. J. Andrade, M. J. Schöning, and J. Wang, "Epidermal tattoo potentiometric sodium sensors with wireless signal transduction for continuous non-invasive sweat monitoring," *Biosensors and Bioelectronics*, vol. 54, pp. 603–609, 4 2014.

[21] A. Martínez-Olmos, J. Fernández-Salmerón, N. Lopez-Ruiz, A. Rivadeneyra Torres, L. F. Capitan-Vallvey, and A. J. Palma, "Screen printed flexible radiofrequency identification tag for oxygen monitoring," *Analytical Chemistry*, vol. 85, no. 22, pp. 11098–11105, 2013.

[22] C. W. Foster, J. P. Metters, D. K. Kampouris, and C. E. Banks, "Ultraflexible screen-printed graphitic electroanalytical sensing platforms," *Electroanalysis*, vol. 26, no. 2, pp. 262–274, 2014.

[23] D.-H. Kim, N. Lu, R. Ma, Y.-S. Kim, R.-H. Kim, S. Wang, J. Wu, S. M. Won, H. Tao, A. Islam, K. J. Yu, T.-i. Kim, R. Chowdhury, M. Ying, L. Xu, M. Li, H.-J. Chung, H. Keum, M. McCormick, P. Liu, Y.-W. Zhang, F. G. Omenetto, Y. Huang, T. Coleman, and J. A. Rogers, "Epidermal Electronics," *Science*, vol. 333, pp. 838–843, 8 2011.

[24] D. H. Kim, Y. S. Kim, J. Wu, Z. Liu, J. Song, H. S. Kim, Y. Y. Huang, K. C. Hwang, and J. A. Rogers, "Ultrathin silicon circuits with strain-isolation layers and mesh layouts for high-performance electronics on fabric, vinyl, leather, and paper," *Advanced Materials*, vol. 21, no. 36, pp. 3703–3707, 2009.

[25] M. Ying, A. P. Bonifas, N. Lu, Y. Su, R. Li, H. Cheng, A. Ameen, Y. Huang, and J. a. Rogers, "Silicon nanomembranes for fingertip electronics," *Nanotechnology*, vol. 23, no. 34, p. 344004, 2012.

[26] D. Son, J. Lee, S. Qiao, R. Ghaffari, J. Kim, J. E. Lee, C. Song, S. J. Kim, D. J. Lee, S. W. Jun, S. Yang, M. Park, J. Shin, K. Do, M. Lee, K. Kang, C. S. Hwang, N. Lu, T. Hyeon, and D.-H. Kim, "Multifunctional wearable devices for diagnosis and therapy of movement disorders.," *Nature nanotechnology*, vol. 9, no. 5, pp. 397–404, 2014.

[27] K.-I. Jang, H. U. Chung, S. Xu, C. H. Lee, H. Luan, J. Jeong, H. Cheng, G.-T. Kim, S. Y. Han, J. W. Lee, J. Kim, M. Cho, F. Miao, Y. Yang, H. N. Jung, M. Flavin, H. Liu, G. W. Kong, K. J. Yu, S. I. Rhee, J. Chung, B. Kim, J. W. Kwak, M. H. Yun, J. Y. Kim, Y. M. Song, U. Paik, Y. Zhang, Y. Huang, and J. A. Rogers, "Soft network composite materials with deterministic and bio-inspired designs," *Nature Communications*, vol. 6, p. 6566, 3 2015.

[28] S. Xu, Y. Zhang, J. Cho, J. Lee, X. Huang, L. Jia, J. a. Fan, Y. Su, J. Su, H. Zhang, H. Cheng, B. Lu, C. Yu, C. Chuang, T.-I. Kim, T. Song,

K. Shigeta, S. Kang, C. Dagdeviren, I. Petrov, P. V. Braun, Y. Huang, U. Paik, and J. a. Rogers, "Stretchable batteries with self-similar serpentine interconnects and integrated wireless recharging systems," *Nature Communications*, vol. 4, p. 1543, 2 2013.

[29] J. W. Jeong, M. K. Kim, H. Cheng, W. H. Yeo, X. Huang, Y. Liu, Y. Zhang, Y. Huang, and J. A. Rogers, "Capacitive epidermal electronics for electrically safe, long-term electrophysiological measurements," *Advanced Healthcare Materials*, vol. 3, pp. 642–648, 10 2014.

[30] J. Kim, A. Banks, H. Cheng, Z. Xie, S. Xu, K. I. Jang, J. W. Lee, Z. Liu, P. Gutruf, X. Huang, P. Wei, F. Liu, K. Li, M. Dalal, R. Ghaffari, X. Feng, Y. Huang, S. Gupta, U. Paik, and J. A. Rogers, "Epidermal electronics with advanced capabilities in near-field communication," *Small*, vol. 11, no. 8, pp. 906–912, 2015.

[31] K.-I. Jang, S. Y. Han, S. Xu, K. E. Mathewson, Y. Zhang, J.-W. Jeong, G.-T. Kim, R. C. Webb, J. W. Lee, T. J. Dawidczyk, R. H. Kim, Y. M. Song, W.-H. Yeo, S. Kim, H. Cheng, S. I. Rhee, J. Chung, B. Kim, H. U. Chung, D. Lee, Y. Yang, M. Cho, J. G. Gaspar, R. Carbonari, M. Fabiani, G. Gratton, Y. Huang, and J. a. Rogers, "Rugged and breathable forms of stretchable electronics with adherent composite substrates for transcutaneous monitoring," *Nature Communications*, vol. 5, p. 4779, 9 2014.

[32] S. K. Lee, B. J. Kim, H. Jang, S. C. Yoon, C. Lee, B. H. Hong, J. A. Rogers, J. H. Cho, and J. H. Ahn, "Stretchable graphene transistors with printed dielectrics and gate electrodes," *Nano Letters*, vol. 11, no. 11, pp. 4642–4646, 2011.

[33] J. Viventi, D.-H. Kim, J. D. Moss, Y.-S. Kim, J. A. Blanco, N. Annetta, A. Hicks, J. Xiao, Y. Huang, D. J. Callans, J. A. Rogers, and B. Litt, "A Conformal, Bio-Interfaced Class of Silicon Electronics for Mapping Cardiac Electrophysiology," *Science Translational Medicine*, vol. 2, pp. 22–24, 3 2010.

[34] J. Viventi, D.-H. Kim, L. Vigeland, E. S. Frechette, J. a. Blanco, Y.-S. Kim, A. E. Avrin, V. R. Tiruvadi, S.-W. Hwang, A. C. Vanleer, D. F. Wulsin, K. Davis, C. E. Gelber, L. Palmer, J. Van der Spiegel, J. Wu, J. Xiao, Y. Huang, D. Contreras, J. a. Rogers, and B. Litt, "Flexible, foldable, actively multiplexed, high-density electrode array for mapping brain activity in vivo.," *Nature neuroscience*, vol. 14, no. 12, pp. 1599–605, 2011.

[35] T. Li, Z. Suo, S. P. Lacour, and S. Wagner, "Compliant thin film patterns of stiff materials as platforms for stretchable electronics," *Journal of Materials Research*, vol. 20, pp. 3274–3277, 12 2005.

[36] T. Ware, D. Simon, K. Hearon, C. Liu, S. Shah, J. Reeder, N. Khodaparast, M. P. Kilgard, D. J. Maitland, R. L. Rennaker, and W. E. Voit, "Three-Dimensional Flexible Electronics Enabled by Shape Memory Polymer Substrates for Responsive Neural Interfaces," *Macromolecular Materials and Engineering*, vol. 297, pp. 1193–1202, 12 2012.

[37] D. Simon, T. Ware, R. Marcotte, B. R. Lund, D. W. Smith, M. Di Prima, R. L. Rennaker, and W. Voit, "A comparison of polymer substrates for photolithographic processing of flexible bioelectronics," *Biomedical Microdevices*, vol. 15, pp. 925–939, 12 2013.

[38] D. J. Lipomi, M. Vosgueritchian, B. C.-K. Tee, S. L. Hellstrom, J. a. Lee, C. H. Fox, and Z. Bao, "Skin-like pressure and strain sensors based on transparent elastic films of carbon nanotubes.," *Nature nanotechnology*, vol. 6, no. 12, pp. 788–92, 2011.

[39] G. Schwartz, B. C.-K. Tee, J. Mei, A. L. Appleton, D. H. Kim, H. Wang, and Z. Bao, "Flexible polymer transistors with high pressure sensitivity for application in electronic skin and health monitoring," *Nature Communications*, vol. 4, p. 1859, 5 2013.

[40] M. Kaltenbrunner, T. Sekitani, J. Reeder, T. Yokota, K. Kuribara, T. Tokuhara, M. Drack, R. Schwödiauer, I. Graz, S. Bauer-Gogonea, S. Bauer, and T. Someya, "An ultra-lightweight design for imperceptible plastic electronics.," *Nature*, vol. 499, no. 7459, pp. 458–63, 2013.

[41] G. S. Jeong, D.-H. Baek, H. C. Jung, J. H. Song, J. H. Moon, S. W. Hong, I. Y. Kim, and S.-H. Lee, "Solderable and electroplatable flexible electronic circuit on a porous stretchable elastomer," *Nature Communications*, vol. 3, no. May, p. 977, 2012.

[42] S. R. Forrest, "The path to ubiquitous and low-cost organic electronic appliances on plastic," *Nature*, vol. 428, pp. 911–918, 4 2004.

[43] S. H. Kim, J. Yoon, S. O. Yun, Y. Hwang, H. S. Jang, and H. C. Ko, "Ultrathin sticker-type ZnO thin film transistors formed by transfer printing via topological confinement of water-soluble sacrificial polymer in dimple structure," *Advanced Functional Materials*, vol. 23, no. 11, pp. 1475–1482, 2013.

[44] V. Linder, B. D. Gates, D. Ryan, B. a. Parviz, and G. M. Whitesides, "Water-soluble sacrificial layers for surface micromachining," *Small*, vol. 1, pp. 730–736, 2005.

[45] K. H. Yim, Z. Zheng, Z. Liang, R. H. Friend, W. T. S. Huck, and J. S. Kim, "Efficient conjugated-polymer optoelectronic devices fabricated by thin-film transfer-printing technique," *Advanced Functional Materials*, vol. 18, pp. 1012–1019, 2008.

[46] B. Zhao, G. Ji, and X. Gao, "Transfer printing of magnetic structures with enhanced performance using a new type of water-soluble sacrificial layer," *RSC Adv.*, vol. 5, no. 70, pp. 56959–56966, 2015.

[47] A. Carlson, A. M. Bowen, Y. Huang, R. G. Nuzzo, and J. A. Rogers, "Transfer printing techniques for materials assembly and micro/nanodevice fabrication," *Advanced Materials*, vol. 24, pp. 5284–5318, 10 2012.

[48] W. H. Yeo, Y. S. Kim, J. Lee, A. Ameen, L. Shi, M. Li, S. Wang, R. Ma, S. H. Jin, Z. Kang, Y. Huang, and J. A. Rogers, "Multifunctional epidermal electronics printed directly onto the skin," *Advanced Materials*, vol. 25, no. 20, pp. 2773–2778, 2013.

[49] D. O'Halloran and E. Kvochko, "Industrial Internet of Things: Unleashing the Potential of Connected Products and Services," Tech. Rep. January, 2015.

[50] L. Atzori, A. Iera, and G. Morabito, "The Internet of Things: A survey," *Computer Networks*, vol. 54, pp. 2787–2805, 10 2010.

[51] K. S. Novoselov, "Electric Field Effect in Atomically Thin Carbon Films," *Science*, vol. 306, pp. 666–669, 10 2004.

[52] K. Fujita, T. Yasuda, and T. Tsutsui, "Flexible organic field-effect transistors fabricated by the electrode-peeling transfer with an assist of self-assembled monolayer," *Applied Physics Letters*, vol. 82, pp. 4373–4375, 6 2003.

[53] B. Ilic and H. G. Craighead, "Topographical Patterning of Chemically Sensitive Biological Materials Using a Polymer-Based Dry Lift Off," *Biomedical Microdevices*, vol. 2, no. 4, pp. 317–322, 2000.

[54] J. A. DeFranco, B. S. Schmidt, M. Lipson, and G. G. Malliaras, "Photolithographic patterning of organic electronic materials," *Organic Electronics*, vol. 7, pp. 22–28, 2 2006.

[55] M. E. Grady, P. H. Geubelle, and N. R. Sottos, "Interfacial adhesion of photode fi nable polyimide fi lms on passivated silicon," *Thin Solid Films*, vol. 552, pp. 116–123, 2014.

[56] J. Yoon, A. J. Baca, S.-I. Park, P. Elvikis, J. B. Geddes, L. Li, R. H. Kim, J. Xiao, S. Wang, T.-H. Kim, M. J. Motala, B. Y. Ahn, E. B. Duoss, J. a.

Lewis, R. G. Nuzzo, P. M. Ferreira, Y. Huang, A. Rockett, and J. a. Rogers, "Ultrathin silicon solar microcells for semitransparent, mechanically flexible and microconcentrator module designs," *Nature Materials*, vol. 7, pp. 907–915, 11 2008.

[57] S. I. Park, Y. Xiong, R. H. Kim, P. Elvikis, M. Meitl, D. H. Kim, J. Wu, J. Yoon, C. J. Yu, Z. Liu, Y. Huang, K. C. Hwang, P. Ferreira, X. Li, K. Choquette, and J. A. Rogers, "Printed assemblies of inorganic light-emitting diodes for deformable and semitransparent displays," *Science*, vol. 325, no. 5943, pp. 977–981, 2009.

[58] H. J. Chung, T. I. Kim, H. S. Kim, S. A. Wells, S. Jo, N. Ahmed, Y. H. Jung, S. M. Won, C. A. Bower, and J. A. Rogers, "Fabrication of releasable single-crystal silicon-metal oxide field-effect devices and their deterministic assembly on foreign substrates," *Advanced Functional Materials*, vol. 21, no. 16, pp. 3029–3036, 2011.

[59] D. W. van Krevelen and K. Te Nijenhuis, *Properties of polymers*. Amsterdam: Elsevier, 4 ed., 2009.

[60] N. Bowden, S. Brittain, A. G. Evans, J. W. Hutchinson, and G. M. Whitesides, "Spontaneous formation of ordered structures in thin films of metals supported on an elastomeric polymer," *Nature*, vol. 393, pp. 146–149, 5 1998.

[61] W. T. S. Huck, N. Bowden, P. Onck, T. Pardoen, J. W. Hutchinson, and G. M. Whitesides, "Ordering of spontaneously formed buckles on planar surfaces," *Langmuir*, vol. 16, no. 7, pp. 3497–3501, 2000.

[62] S. P. Lacour, J. Jones, S. Wagner, T. Li, and Z. Suo, "Stretchable Interconnects for Elastic Electronic Surfaces," *Proceedings of the IEEE*, vol. 93, no. 8, pp. 1459–1466, 2005.

[63] T. Adrega and S. P. Lacour, "Stretchable gold conductors embedded in PDMS and patterned by photolithography: fabrication and electromechanical characterization," *Journal of Micromechanics and Microengineering*, vol. 20, no. 5, p. 055025, 2010.

[64] E. Niedermeyer and F. H. Lopes da Silva, *Electroencephalography: Basic Principles, Clinical Applications, and Related Fields*, vol. 1. Philadelphia: Lippincott Williams & Wilkins, 2004.

[65] E. T. McAdams, J. Jossinet, R. Subramanian, and R. G. E. McCauley, "Characterization of gold electrodes in phosphate buffered saline solution by impedance and noise measurements for biological applications," in *Annual International Conference of the IEEE Engineering in Medicine and Biology - Proceedings*, vol. 1, pp. 4594–4597, 1 2006.

[66] P. Tallgren, S. Vanhatalo, K. Kaila, and J. Voipio, "Evaluation of commercially available electrodes and gels for recording of slow EEG potentials," *Clinical Neurophysiology*, vol. 116, pp. 799–806, 4 2005.

[67] D. Ba, B. Babadi, P. L. Purdon, and E. N. Brown, "Robust spectrotemporal decomposition by iteratively reweighted least squares," *Proceedings of the National Academy of Sciences*, vol. 111, no. 50, pp. E5336–E5345, 2014.

[68] L.-D. Liao, I.-J. Wang, S.-F. Chen, J.-Y. Chang, and C.-T. Lin, "Design, Fabrication and Experimental Validation of a Novel Dry-Contact Sensor for Measuring Electroencephalography Signals without Skin Preparation," *Sensors*, vol. 11, pp. 5819–5834, 5 2011.

[69] J. Zhou, Y. Gu, P. Fei, W. Mai, Y. Gao, R. Yang, G. Bao, and Z. L. Wang, "Flexible piezotronic strain sensor," *Nano Letters*, vol. 8, no. 9, pp. 3035–3040, 2008.

[70] N.-K. Chang, C.-C. Su, and S.-H. Chang, "Fabrication of single-walled carbon nanotube flexible strain sensors with high sensitivity," *Applied Physics Letters*, vol. 92, no. 6, p. 063501, 2008.

[71] J. N. Patel, B. Kaminska, B. L. Gray, and B. D. Gates, "A sacrificial SU-8 mask for direct metallization on PDMS," *Journal of Micromechanics and Microengineering*, vol. 19, p. 115014, 11 2009.

[72] J. N. Patel, B. Kaminska, B. L. Gray, and B. D. Gates, "PDMS as a sacrificial substrate for SU-8-based biomedical and microfluidic applications," *Journal of Micromechanics and Microengineering*, vol. 18, p. 095028, 9 2008.

[73] M. Melzer, D. Karnaushenko, G. Lin, S. Baunack, D. Makarov, and O. G. Schmidt, "Direct transfer of magnetic sensor devices to elastomeric supports for stretchable electronics," *Advanced Materials*, vol. 27, no. 8, pp. 1333–1338, 2015.

[74] J. C. McDonald, D. C. Duffy, J. R. Anderson, D. T. Chiu, H. Wu, O. J. A. Schueller, and G. M. Whitesides, "Fabrication of microfluidic systems in poly (dimethylsiloxane)," *Electrophoresis*, vol. 21, no. 1, pp. 27–40, 2000.

[75] H. Schmid, H. Wolf, R. Allenspach, H. Riel, S. Karg, B. Michel, and E. Delamarche, "Preparation of metallic films on elastomeric stamps and their application for contact processing and contact printing," *Advanced Functional Materials*, vol. 13, pp. 145–153, 2 2003.

[76] Y. Sun, S. P. Lacour, R. A. Brooks, N. Rushton, J. Fawcett, and R. E. Cameron, "Assessment of the biocompatibility of photosensitive polyimide for implantable medical device use.," *Journal of biomedical materials research. Part A*, vol. 90, no. 3, pp. 648–655, 2009.

[77] M. J. Harbert, S. S. Rosenberg, D. Mesa, M. Sinha, N. P. Karanjia, M. Nespeca, and T. P. Coleman, "Demonstration of the Use of Epidermal Electronics in Neurological Monitoring," *Annals of Neurology*, vol. 74, no. 1, pp. S76–S77, 2013.

[78] D. R. Merrill, M. Bikson, and J. G. Jefferys, "Electrical stimulation of excitable tissue: design of efficacious and safe protocols," *Journal of Neuroscience Methods*, vol. 141, pp. 171–198, 2 2005.

[79] A. Ghomashchi, Z. Zheng, N. Majaj, M. Trumpis, L. Kiorpes, and J. Viventi, "A low-cost, open-source, wireless electrophysiology system," in *2014 36th Annual International Conference of the IEEE Engineering in Medicine and Biology Society, EMBC 2014*, pp. 3138–3141, 2014.

[80] M. A. Escabi, H. L. Read, J. Viventi, D.-H. Kim, N. C. Higgins, D. A. Storace, A. S. K. Liu, A. M. Gifford, J. F. Burke, M. Campisi, Y.-S. Kim, A. E. Avrin, V. d. Spiegel Jan, Y. Huang, M. Li, J. Wu, J. A. Rogers, B. Litt, and Y. E. Cohen, "A high-density, high-channel count, multiplexed ECoG array for auditory-cortex recordings," *Journal of Neurophysiology*, vol. 112, no. 6, pp. 1566–1583, 2014.

[81] P. P. Mercier, A. C. Lysaght, S. Bandyopadhyay, A. P. Chandrakasan, and K. M. Stankovic, "Energy extraction from the biologic battery in the inner ear," *Nature Biotechnology*, vol. 30, no. 12, pp. 1240–1243, 2012.

[82] Presidents Council of Advisors on Science and Technology, "REPORT TO THE PRESIDENT: ACCELERATING U.S. ADVANCED MANUFACTURING," tech. rep., Washington D. C., 10 2014.

[83] N. Patrito, J. M. McLachlan, S. N. Faria, J. Chan, and P. R. Norton, "A novel metal-protected plasma treatment for the robust bonding of polydimethylsiloxane," *Lab on a Chip*, vol. 7, no. 12, pp. 1813–1818, 2007.

[84] K. Efimenko, W. E. Wallace, and J. Genzer, "Surface Modification of Sylgard-184 Poly(dimethyl siloxane) Networks by Ultraviolet and Ultraviolet/Ozone Treatment," *Journal of Colloid and Interface Science*, vol. 254, no. 2, pp. 306–315, 2002.

[85] B. T. Ginn and O. Steinbock, "Polymer Surface Modification Using Microwave-Oven-Generated Plasma," *Langmuir*, vol. 19, pp. 8117–8118, 9 2003.

[86] D. Armani, C. Liu, and N. Aluru, "Re-configurable fluid circuits by PDMS elastomer micromachining," in *Technical Digest. IEEE International MEMS 99 Conference. Twelfth IEEE International Conference on Micro Electro Mechanical Systems (Cat. No.99CH36291)*, pp. 222–227, IEEE, 1999.

[87] D. Y. Kang, P. N. Deyoung, A. Malhotra, R. L. Owens, and T. P. Coleman, "A State Space and Density Estimation Framework for Sleep Staging in Obstructive Sleep Apnea," *In Press, IEEE Transactions on Biomedical Engineering*, 2017.

[88] R. B. Berry, R. Brooks, C. E. Gamaldo, S. Harding, C. L. Marcus, and B. V. Vaughn, "The AASM manual for the scoring of sleep and associated events," *Rules, Terminology and Technical Specifications, Darien, Illinois, American Academy of Sleep Medicine*, 2012.

[89] R. Agarwal and J. Gotman, "Computer-assisted sleep staging," *IEEE Transactions on Biomedical Engineering*, vol. 48, no. 12, pp. 1412–1423, 2001.

[90] J. Virkkala, J. Hasan, A. Värri, S. L. Himanen, and K. Müller, "Automatic sleep stage classification using two-channel electro-oculography," *Journal of Neuroscience Methods*, vol. 166, no. 1, pp. 109–115, 2007.

[91] S.-F. Liang, C.-E. Kuo, Y.-H. Hu, and Y.-S. Cheng, "A rule-based automatic sleep staging method.," *Journal of Neuroscience Methods*, vol. 205, no. 1, pp. 169–76, 2012.

[92] C. Stepnowsky, D. Levendowski, D. Popovic, I. Ayappa, and D. M. Rapoport, "Scoring accuracy of automated sleep staging from a bipolar electroocular recording compared to manual scoring by multiple raters," *Sleep Medicine*, vol. 14, no. 11, pp. 1199–1207, 2013.

[93] A. Malhotra, M. Younes, S. T. Kuna, R. Benca, C. a. Kushida, J. Walsh, A. Hanlon, B. Staley, A. I. Pack, and G. W. Pien, "Performance of an automated polysomnography scoring system versus computer-assisted manual scoring.," *Sleep*, vol. 36, pp. 573–82, 4 2013.

[94] B. Koley and D. Dey, "An ensemble system for automatic sleep stage classification using single channel EEG signal," *Computers in Biology and Medicine*, vol. 42, no. 12, pp. 1186–1195, 2012.

[95] G. Zhu, Y. Li, and P. P. Wen, "Analysis and classification of sleep stages based on difference visibility graphs from a single-channel EEG signal," *IEEE Journal of Biomedical and Health Informatics*, vol. 18, no. 6, pp. 1813–1821, 2014.

[96] M. Radha, G. Garcia-Molina, M. Poel, and G. Tononi, "Comparison of feature and classifier algorithms for online automatic sleep staging based on a single EEG signal," in *2014 36th Annual International Conference of the IEEE Engineering in Medicine and Biology Society*, vol. 2014, pp. 1876–1880, IEEE, 8 2014.

[97] V. Bajaj and R. B. Pachori, "Automatic classification of sleep stages based on the time-frequency image of EEG signals," *Computer Methods and Programs in Biomedicine*, vol. 112, pp. 320–328, 12 2013.

[98] A. Flexer, G. Gruber, and G. Dorffner, "A reliable probabilistic sleep stager based on a single EEG signal," *Artificial Intelligence in Medicine*, vol. 33, no. 3, pp. 199–207, 2005.

[99] L. G. Doroshenkov, V. a. Konyshev, and S. V. Selishchev, "Classification of human sleep stages based on EEG processing using hidden Markov models," *Meditsinskaia tekhnika*, vol. 41, no. 1, pp. 24–28, 2007.

[100] M. T. Bianchi, N. A. Eiseman, S. S. Cash, J. Mietus, C. K. Peng, and R. J. Thomas, "Probabilistic sleep architecture models in patients with and without sleep apnea," *Journal of Sleep Research*, vol. 21, no. 3, pp. 330–341, 2012.

[101] S.-T. Pan, C.-E. Kuo, J.-H. Zeng, and S.-F. Liang, "A transition-constrained discrete hidden Markov model for automatic sleep staging," *BioMedical Engineering OnLine*, vol. 11, no. 1, p. 52, 2012.

[102] F. Yaghouby and S. Sunderam, "Quasi-supervised scoring of human sleep in polysomnograms using augmented input variables," *Computers in Biology and Medicine*, vol. 59, pp. 54–63, 2015.

[103] J. A. Onton, D. Y. Kang, and T. P. Coleman, "Visualization of Whole-Night Sleep EEG From 2-Channel Mobile Recording Device Reveals Distinct Deep Sleep Stages with Differential Electrodermal Activity," *Frontiers in Human Neuroscience*, vol. 10, p. 605, 11 2016.

[104] J. R. Shambroom, S. E. Fábregas, and J. Johnstone, "Validation of an automated wireless system to monitor sleep in healthy adults," *Journal of Sleep Research*, vol. 21, no. 2, pp. 221–230, 2012.

[105] Y.-L. Hsu, Y.-T. Yang, J.-S. Wang, and C.-Y. Hsu, "Automatic sleep stage recurrent neural classifier using energy features of EEG signals," *Neurocomputing*, vol. 104, pp. 105–114, 3 2013.

[106] L. Fraiwan, K. Lweesy, N. Khasawneh, H. Wenz, and H. Dickhaus, "Automated sleep stage identification system based on time-frequency analysis of a single EEG channel and random forest classifier," *Computer Methods and Programs in Biomedicine*, vol. 108, no. 1, pp. 10–19, 2012.

[107] G. Garcia-Molina, M. Bellesi, S. Pastoor, S. Pfundtner, B. Riedner, and G. Tononi, "Online single EEG channel based automatic sleep staging," *Lecture Notes in Computer Science (including subseries Lecture Notes in Ar-*

tificial Intelligence and Lecture Notes in Bioinformatics), vol. 8020 LNAI, no. PART 2, pp. 333–342, 2013.

[108] C. Lainscsek, V. Messager, A. Portman, J.-F. Muir, T. J. Sejnowski, and C. Letellier, "Automatic Sleep Scoring from a Single Electrode Using Delay Differential Equations," in *Nonlinear Dynamics and Systems Theory* (J. Awrejcewicz, ed.), vol. 15 of *Springer Proceedings in Mathematics & Statistics*, pp. 371–382, Cham: Springer International Publishing, 2014.

[109] A. R. Hassan, S. K. Bashar, and M. I. H. Bhuiyan, "On the classification of sleep states by means of statistical and spectral features from single channel Electroencephalogram," in *2015 International Conference on Advances in Computing, Communications and Informatics, ICACCI 2015*, pp. 2238–2243, 2015.

[110] B. Kemp, A. H. Zwinderman, B. Tuk, H. A. C. Kamphuisen, and J. J. L. Oberyé, "Analysis of a sleep-dependent neuronal feedback loop: The slow-wave microcontinuity of the EEG," *IEEE Transactions on Biomedical Engineering*, vol. 47, no. 9, pp. 1185–1194, 2000.

[111] A. L. Goldberger, L. A. N. Amaral, L. Glass, J. M. Hausdorff, P. C. Ivanov, R. G. Mark, J. E. Mietus, G. B. Moody, C.-K. Peng, and H. E. Stanley, "PhysioBank, PhysioToolkit, and PhysioNet: Components of a New Research Resource for Complex Physiologic Signals," *Circulation*, vol. 101, pp. e215–e220, 6 2000.

[112] D. Thomson, "Spectrum estimation and harmonic analysis," *Proceedings of the IEEE*, vol. 70, no. 9, pp. 1055–1096, 1982.

[113] B. Babadi and E. N. Brown, "A review of multitaper spectral analysis," *IEEE Transactions on Biomedical Engineering*, vol. 61, no. 5, pp. 1555–1564, 2014.

[114] M. J. Prerau, R. E. Brown, M. T. Bianchi, J. M. Ellenbogen, and P. L. Purdon, "Sleep Neurophysiological Dynamics Through the Lens of Multitaper Spectral Analysis.," *Physiology (Bethesda, Md.)*, vol. 32, no. 1, pp. 60–92, 2017.

[115] T. P. Bronez, "On the Performance Advantage of Multitaper Spectral Analysis," *IEEE Transactions on Signal Processing*, vol. 40, no. 12, pp. 2941–2946, 1992.

[116] J. L. Cantero, M. Atienza, and R. M. Salas, "Human alpha oscillations in wakefulness, drowsiness period, and REM sleep: Different electroencephalographic phenomena within the alpha band," *Neurophysiologie Clinique*, vol. 32, no. 1, pp. 54–71, 2002.

[117] R. L. Williams, I. Karacan, and C. J. Hursch, *Electroencephalography (EEG) of human sleep: clinical applications*. New York: John Wiley & Sons, 1974.

[118] M. A. Carskadon, E. D. Brown, and W. C. Dement, "Sleep Fragmentation in the Elderly : Relationship to Daytime Sleep Tendency," *Neurobiology of Aging*, vol. 3, pp. 321–327, 1982.

[119] F. Stocchi, L. Barbato, G. Nordera, A. Berardelli, and S. Ruggieri, "Sleep disorders in Parkinsons disease," *Journal of Neurology*, vol. 245, pp. S15–S18, 4 1998.

[120] G. Zamir, J. Press, A. Tal, and A. Tarasiuk, "Sleep fragmentation in children with juvenile rheumatoid arthritis," *Journal of Rheumatology*, vol. 6, no. 25, p. 11911197, 1998.

[121] D. J. Eckert, A. Malhotra, A. Wellman, and D. P. White, "Trazodone increases the respiratory arousal threshold in patients with obstructive sleep apnea and a low arousal threshold.," *Sleep*, vol. 37, no. 4, pp. 811–9, 2014.

[122] D. W. Scott, "On optimal and data-based histograms," *Biometrika*, vol. 66, no. 3, pp. 605–610, 1979.

[123] L. R. Rabiner and B. H. Juang, "An Introduction to Hidden Markov Models," *IEEE ASSP Magazine*, vol. 3, no. 1, pp. 4–16, 1986.

[124] C.-C. Lo, R. P. Bartsch, and P. C. Ivanov, "Asymmetry and Basic Pathways in Sleep-Stage Transitions.," *Europhysics letters*, vol. 102, no. 1, p. 10008, 2013.

[125] J. Cohen, "A coefficient of agreement for nomial scales," *Educational and Psychological Measurement*, vol. 20, no. 1, pp. 37–46, 1960.

[126] J. R. Landis and G. G. Koch, "The Measurement of Observer Agreement for Categorical Data," *Biometrics*, vol. 33, no. 1, pp. 159–174, 1977.

[127] M. H. Silber, S. Ancoli-Israel, M. H. Bonnet, S. Chokroverty, M. M. Grigg-Damberger, M. Hirshkowitz, S. Kapen, S. A. Keenan, M. H. Kryger, T. Penzel, M. R. Pressman, and C. Iber, "The visual scoring of sleep in adults," *Journal of Clinical Sleep Medicine*, vol. 3, no. 2, pp. 121–131, 2007.

[128] A. Feinstein and D. Cicchetti, "High Agreement But Low Kappa : I . the Problems of Two Paradoxes *," *Journal of Clinical Epidemiology*, vol. 43, no. 6, pp. 543–549, 1990.

[129] M. Younes, M. Younes, and E. Giannouli, "Accuracy of Automatic Polysomnography Scoring Using Frontal Electrodes," *Journal of Clinical Sleep Medicine*, vol. 12, pp. 735–746, 5 2016.

[130] M. Jobert, E. Poiseau, P. Jähnig, H. Schulz, and S. Kubicki, "Pattern Recognition by Matched Filtering: An Analysis of Sleep Spindle and K-Complex Density under the Influence of Lormetazepam and Zopiclone," *Neuropsychobiology*, vol. 26, pp. 100–107, 1992.

[131] G. M. Hatzilabrou, N. Greenberg, R. J. Sclabassi, T. Carroll, R. D. Guthrie, and M. S. Scher, "A comparison of conventional and matched filtering techniques for rapid eye movement detection of the newborn," *IEEE Transactions on Biomedical Engineering*, vol. 41, no. 10, pp. 990–995, 1994.

[132] H.-L. C. Kao, C. Holz, A. Roseway, A. Calvo, and C. Schmandt, "DuoSkin," in *Proceedings of the 2016 ACM International Symposium on Wearable Computers - ISWC '16*, (New York, New York, USA), pp. 16–23, ACM Press, 2016.

[133] T. Y. Kim, S. A. Hong, and S. Yang, "A Solid-State Thin-Film Ag/AgCl Reference Electrode Coated with Graphene Oxide and Its Use in a pH Sensor," *Sensors*, vol. 15, no. 3, pp. 6469–6482, 2015.

[134] Y.-S. Kim, J. Lu, B. Shih, A. Gharibans, Z. Zou, K. Matsuno, R. Aguilera, J. Xiao, Y. Han, A. Meek, M. T. Tolley, and T. P. Coleman, "Scalable Manufacturing of Solderable and Stretchable Physiologic Sensing Systems," *Advanced Materials*, 2017.

[135] A. A. Gharibans, S. Kim, D. C. Kunkel, and T. P. Coleman, "High-Resolution Electrogastrogram: A Novel, Noninvasive Method for Determining Gastric Slow-Wave Direction and Speed," *IEEE Transactions on Biomedical Engineering*, vol. 64, pp. 807–815, 4 2017.